Impacts of water advection and CO_2 exchange on the carbon dioxide removal potential of ocean alkalinity enhancement

Charly A. Moras[1], Matias Saez Moreno[1], Peggy Bartsch[1], Jens Hartmann[1]

[1]Department of Earth System Sciences, University of Hamburg, Hamburg, Germany

Correspondence to: Charly A. Moras (charly.moras@uni-hamburg.de)

Abstract. Ocean alkalinity enhancement (OAE) is a carbon dioxide removal strategy with high carbon dioxide (CO_2) uptake potential and moderate cost. Long-term implementation has been assessed in modelling studies, but most laboratory experiments have focused on short time frames with strong advection, which may not be representative of natural systems. Hence, the long-term fate of added alkalinity has yet to be fully addressed in laboratory experiments. Furthermore, the role of CO_2 ingassing on overall efficiency is still largely overlooked. In a new setup, six-month experiments were conducted using seawater amended with solid $Ca(OH)_2$ and $Mg(OH)_2$ and liquid NaOH, with a constant atmospheric CO_2 supply. Bottles were either kept stagnant or exposed to slow circular advection, yielding gas-transfer-velocity equivalent wind speed of ~3 m s^{-1}. All experiments revealed smaller measured increases in total alkalinity than expected, but in the bottles subjected to advection, alkalinity generation was nearly twice as high in some cases and CO_2 ingassing rates were significantly faster. This led to a faster equilibration, decreasing the high pH/low CO_2 period, recently identified as a potential threat to living organisms. The critical alkalinity period (CAP) is introduced here to represent this critical period of altered carbonate chemistry during which secondary calcium carbonate ($CaCO_3$) formation may occur, significantly altering the CDR potential of the approach. $CaCO_3$ precipitated in most bottles, either as needles when adding $Ca(OH)_2$ or as broccoli-like structures when adding $Mg(OH)_2$. These broccoli-like structures most likely resulted from precipitation on slowly dissolving $Mg(OH)_2$ particles. After the CAP ended, conditions remained stable and freshly precipitated $CaCO_3$ did not redissolve. In addition, when NaOH was used as the alkaline feedstock, $Mg(OH)_2$ flakes were observed but these eventually redissolved in the bottles exposed to advection. The study emphasises the role of water advection on OAE's efficiency and the data presented here may be used to derive lower thresholds for OAE implementation in global models.

Introduction

The increase in atmospheric carbon dioxide (CO_2) concentrations since the Industrial Revolution of the 18th century has been identified as the main cause of global climate change (IPCC, 2022). While strong efforts to reduce CO_2 emissions are required, current projections indicate that these are insufficient to slow down global warming, with active CO_2 removal from the atmosphere being the only solution (Hausfather, 2025; IPCC, 2021). Among the different carbon dioxide removal (CDR) strategies, ocean alkalinity enhancement (OAE) has gained momentum over the past decade as it may offer one of the largest carbon capture potentials, estimated at up to 100 Gt CO_2 ~~(1 Gt CO_2 = 10^{15} g CO_2)~~ per year (Fuss et al., 2026). Through the

dispersal of alkaline materials in coastal areas or in the open ocean, for example, the increase in seawater total alkalinity (TA) allows for more CO_2 to be captured by the ocean (Kheshgi, 1995). However, the question whether added alkalinity remains in the surface ocean and especially whether such alkalinity remains stable long enough to allow for CO_2 equilibration has yet to be fully addressed. Secondary effects such as calcium carbonate ($CaCO_3$) precipitation have recently been identified and may decrease efficiency and possibly lead to CO_2 emissions from the ocean (Fuhr et al., 2022; Moras et al., 2022; Rigopoulos et al., 2018). Early work using olivine-rich minerals revealed that in the presence of particles, increasing alkalinity may trigger $CaCO_3$ formation on the undissolved particles despite slow dissolution kinetics (Fuhr et al., 2022; Rigopoulos et al., 2018). Laboratory s~~S~~tudies using more reactive solid feedstocks such as calcium hydroxide ($Ca(OH)_2$) and magnesium hydroxide ($Mg(OH)_2$), mostly conducted in natural seawater at room temperature, have revealed $CaCO_3$ precipitation once alkalinity was increased by ~500 µmol kg^{-1} (Hartmann et al., 2023; Moras et al., 2022; Moras et al., 2024; Suitner et al., 2024; Varliero et al., 2024).

During the dissolution of powdered alkaline minerals, the micro-environment formed around the alkaline particles likely reaches very high aragonite saturation states (Ω_A), under which aragonite may precipitate. Aragonite precipitation may occur homogeneously from the water column or heterogeneously using undissolved particles as nuclei (Marion et al., 2009). Once precipitation starts, it may enter a runaway pattern, with an increasing precipitation rate, sometimes reaching TA values lower than the starting conditions (Moras et al., 2022). Under some circumstances, the presence of inhibitors such as magnesium (Mg^{2+}) or dissolved organic matter may delay or decrease the precipitation rate (Chave and Suess, 1970; Pan et al., 2021). Hence, $Mg(OH)_2$ could be a more favourable alkaline feedstock than $Ca(OH)_2$, as the Mg^{2+} released from $Mg(OH)_2$ dissolution could inhibit $CaCO_3$ formation, while $Ca(OH)_2$ could allow for early nucleation due to the lattice compatibility of $CaCO_3$ for such particles (Moras et al., 2022; Pan et al., 2021; Tang et al., 2020). Overall, the persistence of high alkalinity and Ω_A ~~(~~micro-~~)~~environments around dissolving particles is expected to enhance the likelihood of $CaCO_3$ formation, particularly through secondary precipitation in the diffusive boundary layer of dissolving particles or on suspended solids (Moras et al., 2022). Also, the concomitant high pH and low CO_2 bulk seawater conditions resulting from alkalinity addition may impact biological processes because CO_2 is essential for photosynthesis (Bach et al., 2019). This transient period following alkalinity addition, during which carbonate chemistry ~~is~~ remains substantially perturbed relative to ambient conditions~~,~~ promotes secondary mineral formation, may affect biological processes, and is hereafter referred to as the critical alkalinity period (CAP). During the CAP, elevated pH and Ω_A together with reduced dissolved CO_2 concentrations increase the likelihood of secondary $CaCO_3$ formation and the duration of biological exposure to unfavourable conditions. The CAP ends once carbonate chemistry progressively returns to conditions comparable to those prior to alkalinity addition, particularly via atmospheric CO_2 invasion and physical dilution. Hence, CAP duration is influenced by the nature and amount of alkaline feedstock used, hydrodynamic conditions, i.e., mixing and dilution, particle settling and CO_2 equilibration, making it an important consideration for safe and effective implementation of OAE.

Previous OAE-focused laboratory experiments with $Ca(OH)_2$ and $Mg(OH)_2$ have been run in a variety of settings. First, these experiments were usually conducted over shorter periods of time, from minutes to weeks (Hartmann et al., 2023; Moras et al.,

2022; Moras et al., 2024; Shaw et al., 2025; Yang et al., 2023), though longer experiments exist with slower-dissolving materials such as olivine-rich minerals (Flipkens et al., 2023; Fuhr et al., 2022; Fuhr et al., 2024; Fuhr et al., 2025; Montserrat et al., 2017). Hence, the longer-term alkalinity stability of hydroxide-based OAE is yet to be fully addressed. Given the time dependency of $CaCO_3$ precipitation kinetics, previously reported patterns for weeks may be different once monitored for months. Second, experiments using hydroxides were mostly conducted using stir bars in closed reaction vessels. While these settings allow for easy and standardised comparison between the various dissolution rates of alkaline minerals and possible precipitation of $CaCO_3$, they generally do not account the role of atmospheric CO_2 ingassing for the stability of alkalinity. Hence, we hypothesise that the patterns observed in closed laboratory experiments with stir bar may not fully represent open-ocean conditions. Here, in a new approach, the dissolution of $Ca(OH)_2$ and $Mg(OH)_2$ in natural seawater was investigated both in static and advected reaction vessels for six months. Circular advection regimes were chosen to try and reproduce turbulent conditions similar to those observed in the open ocean, allowing for vertical diffusion but limiting disruption of the water surface, while gas exchange was allowed to occur during the experiments. Carbonate chemistry was monitored throughout, particle analyses were conducted at the end of the experiments, and recorded changes in dissolved inorganic carbon (DIC) were used to calculate the gas transfer velocities. We later derived the equivalent open ocean wind speeds and compared them with values recorded in the open ocean.

Material and methods

Experimental setup, selection of the revolutions per minute (RPM) and evaporation compensation

Two sets of 42 bottles (1 L wide-mouth polypropylene) each were used to conduct the experiments at room temperature (24.6 ±1.4 °C). About 90 L of natural Indian Ocean seawater was collected from the surface ~400 km southeast of Sri Lanka (2°59.995'N, 77°59.997'E) and stored in five 18 L borosilicate 3.3 glass bottles. The bottles were stored in the dark in a refrigerated container until delivery ~10 weeks after collection. The entire amount of seawater was sterile filtered using a Whatman Polycap 36 AS encapsulated filter with a 0.2 µm pore size. The seawater was stored in a cleaned and MilliQ-rinsed 210 L PP rainwater tank (Garantia rainwater green round barrel). The seawater was bubbled for a week using MilliQ-saturated ambient air following Moras et al. (2023) to allow for the entire content of the tank to be equilibrated with atmospheric pCO_2. The experiments were conducted in 1 L PP bottles that were cleaned in a 3-step process. They were first soaked overnight in a 1% solution of NaOH with dishwashing tablets. The next day, the bottles were rinsed with tap water three times and soaked overnight in a 0.5% solution of HCl. Finally, all bottles were rinsed with tap water and MilliQ (18.2 MΩ) three times each, before being dried overnight in an oven at 60 °C. Each of the 84 cleaned bottles was filled with ~900 g of sterile-filtered seawater and the weight was accurately recorded (balance accuracy ±0.01 g).

One set was placed on a table and kept static throughout the experiments, while the second set was placed on an Edmund Bühler 30 SM C shaking table, set to circular motion at 125 RPM. The choice of motion and RPM was made following a dye test where powdered phenolphthalein dye was added to seawater in a 1 L bottle. The dye changes from a colourless powder to

a bright pinkish colour when dissolved in solutions of pH higher than 8. These experiments revealed that below 80 RPM, the vertical mixing was deemed insufficient, with most of the dye sinking and remaining at the bottom of the bottle. Above 130 RPM, the seawater contained in the bottles reached the rim of the bottle and was deemed too great a risk of spilling. Therefore, a slightly lower rotation rate of 125 RPM was selected, providing suitable particle resuspension yet avoiding water overflow. Similarly, the tests revealed that a circular motion was more appropriate than a linear motion. Linear motion produced insufficient particle resuspension and substantial disruption of the water surface, including splashing. Circular motion produced turbulent conditions with effective vertical mixing without visible splashing. Turbulence can be expressed as a dimensionless number which is also used in physical oceanography, known as the Reynolds number (Reynolds, 1883). To compare turbulence in our experimental setup to naturally occurring ocean turbulence, we derived the Reynolds number from the bottle diameter, tangential velocity, seawater density and dynamic viscosity, as per Griskey (2002). Our conditions yielded a Reynolds number approximately 1.7×10^4, above the threshold considered for turbulent systems (Millero and Poisson, 1981; Thorpe, 2007; Sharqawy, 2010). This setup was used for a total of six months to assess the long-term response of alkalinity addition to seawater.

To minimize evaporation, the headspace of the open bottles was continuously replaced with water-saturated air. For this purpose, air was bubbled through MilliQ contained in a sealed 1 L Schott bottle. Once the air was bubbled through the MilliQ, it was carried over into plastic airflow dividers similar to those used for aquariums (Fig. 1). One tube was positioned in the headspace of each bottle and secured to the bottle neck with binder clips (Fig. A1). The air did not directly bubble the seawater, but rather continuously renewed each bottle headspace with MilliQ-saturated ambient air. To compensate for evaporation, each bottle was regularly weighed, and accurate MilliQ additions were performed when a decrease in weight of more than 5% was observed. To reduce the potential growth of autotrophic organisms, two germicidal UV lamps emitting at 254 nm were mounted on top of the setup and placed so that all bottles were exposed to the UV lights. These lamps were automatically switched on for an hour twice a week in the middle of the night, allowing for a long enough exposure to limit microbial growth.

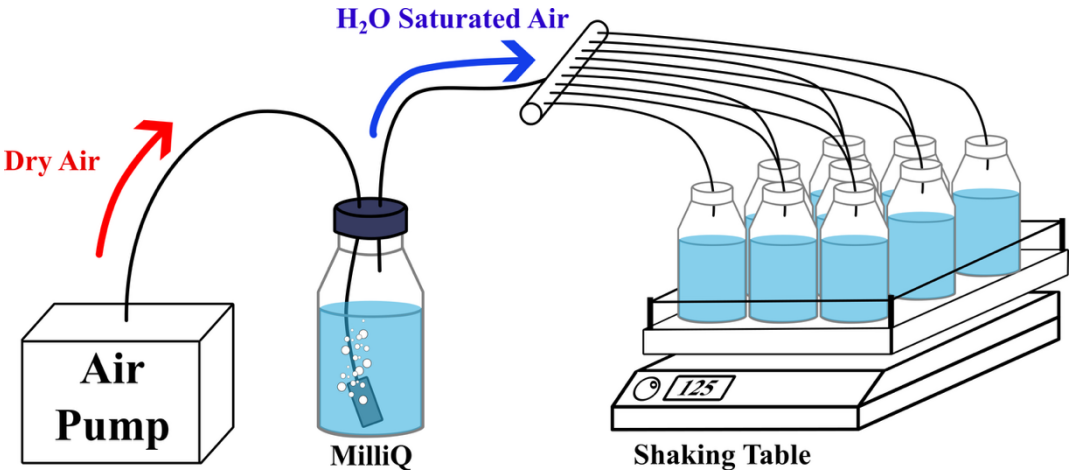

Figure 1: Schematic of the experimental setup. The air pump takes up dry air and pushes it into a closed Schott bottle where MilliQ is bubbled. The newly H_2O-saturated air is then carried to an air diffuser from which individual tubes are connected to each experimental bottle, continuously supplying each open bottle with fresh air equilibrated to atmospheric CO_2.

TA manipulations and sampling procedure

Each of the two 42-bottle experimental sets consisted of three control bottles filled only with sterile-filtered seawater, 18 TA-enhanced bottles with $Ca(OH)_2$ powder, 18 TA-enhanced bottles with $Mg(OH)_2$ powder, and three TA-enhanced bottles with a stock solution of NaOH (Table 1). Every treatment was conducted in triplicate. Targeted alkalinity increases ranged from +100 µmol kg^{-1} to +600 µmol kg^{-1} in increments of 100 µmol kg^{-1} for both alkaline powders, and the NaOH-amended set consisted of a TA increase of +600 µmol kg^{-1}. One bottle was lost from the 125 RPM NaOH treatment after day 6, and one was lost from the 0 RPM NaOH treatment after day 108. Subsequent values therefore represent the means of the two remaining replicates. The alkaline powders $Ca(OH)_2$ and $Mg(OH)_2$ and the NaOH pellets used to make the 1 M NaOH solution were all reagent-grade, obtained from Carl Roth (Germany). The $Ca(OH)_2$ and $Mg(OH)_2$ powders were analysed for grain size distribution with a Bettersizer S3 Plus, exhibiting similar D50 values, i.e., 31.98 and 29.79 µm, respectively, as well as comparable specific surface areas, i.e., 58.90 and 62.82 m^2 kg^{-1}. Both powders were dried overnight at 60 °C, and specific amounts for TA amendments were weighed on weighing paper using a Kern ABT 120-5DNM (± 0.01 mg) balance. $Ca(OH)_2$ additions ranged from 3.67 to 22.26 mg L^{-1}, while $Mg(OH)_2$ additions ranged from 2.88 to 17.54 mg L^{-1} to reach the desired ΔTA targets (Table A 1). The NaOH solution was added using an Eppendorf Research Plus 1000 pipette. Overall, the weighing uncertainty led to an offset between the targeted and estimated TA of less than 1%.

Table 1: Experimental design for one of two sets of 42 bottles, showing the treatment groups (control, $Ca(OH)_2$ powder, $Mg(OH)_2$ powder and NaOH stock solution), amendment levels (expressed in µmol kg^{-1}), and the number of replicate bottles per treatment.

Treatment	+0	+100	+200	+300	+400	+500	+600

Control	3	–	–	–	–	–	–
$Ca(OH)_2$	–	3	3	3	3	3	3
$Mg(OH)_2$	–	3	3	3	3	3	3
NaOH	–	–	–	–	–	–	3

The pH, temperature and conductivity of each sample were measured before manipulation and one, three and six days after alkalinity addition. Thereafter, measurements took place twice a week for the first two months and once a week afterwards. pH and conductivity were measured using a multiparameter pocket measuring device MultiLine Multi 3630 IDS from WTW, with a SenTix 940 pH probe and a WTW TetraCon 925 conductivity probe. The pH probe was calibrated weekly using NIST-traceable buffers and measured values were converted to the total pH scale (pH_T) using measured salinity and temperature and inputting the values into the equation derived by Badocco et al. (2021). The conductivity probe was calibrated before the first measurement to determine the starting salinity of the seawater. Salinity was calculated as 35.346 ±0.077 on the practical salinity scale of 1978 (Lewis and Perkin, 1981).

TA and DIC samples were taken before manipulation to establish background concentrations. Then, sampling occurred on days 1, 3 and 6 after alkalinity addition, and monthly afterwards. Seawater was sampled using a peristaltic pump connected to a 0.2 µm filter from Sartorius. Borosilicate-glass 3.3 TOC vials (24 mL, Shimadzu) were filled slowly from the bottom and allowed to overflow by at least half of their volume (Dickson et al., 2007). The vials were then sealed without headspace using screw caps fitted with red silicone/white PTFE double-layer septa. TA samples were collected immediately after DIC samples, with ~30 mL of water sampled in 100 mL PP bottles. The TA bottles were closed tightly to prevent any evaporation, and both TA and DIC samples were stored refrigerated in the dark until analysis (within one week of sampling). Up to 100 mL was removed at each sampling point, leaving less than 150 mL at the end of the experiment, as the sampled water was not replaced. The remaining water was used for mineral microscopy and elemental composition analysis. For microscopy, about 20 mL of the remaining water was filtered through Whatman polycarbonate Nuclepore filters (0.2 µm) from bottles amended to a target ΔTA of +600 µmol kg^{-1}. The filters were briefly rinsed for several seconds with a few millilitres of fresh MilliQ to remove residual salts before being dried at 60 °C overnight. Another set of filters was used for elemental analysis. ~50 mL of water was accurately weighed and filtered on a Whatman polycarbonate Nuclepore filter (0.2 µm). The recorded weight was used to determine the exact amount of seawater filtered for the analysis. The filter was then placed into a 50 mL Falcon tube to dry overnight. The incubation bottles were rinsed three times with ~15 mL of 3% Suprapure nitric acid to remove precipitates from the bottle walls. The acid was then transferred into the Falcon tube with the filter to dissolve all collected particles before being made up to a final volume of 50 mL.

Carbonate chemistry measurements, mineral analyses and data processing

TA was determined by potentiometric titration using an 888 Titrando connected to an 814 USB Sample Processor (Metrohm) with a 0.02 M HCl solution as the titrant. The titrant ionic strength was adjusted to 0.72 mol kg^{-1} by NaCl addition, corresponding to a salinity of 35 (Dickson et al., 2007). The raw TA values were corrected against certified reference materials (CRM #187) from Dickson (2010). The overall instrument uncertainty was estimated at 0.1% via error propagation of all CRM measurements. DIC analyses were conducted on a Shimadzu TOC-L/CPH analyser calibrated using a CRM (#207). Samples were injected into the reactor filled with fresh 25% H_3PO_4, and the evolved CO_2 was carried by CO_2-free air. The overall instrument uncertainty was also determined via error propagation of all CRM measurements and estimated at 3.5%.

During the six-month experiment, atmospheric CO_2 concentration, temperature and humidity were recorded every 15 minutes with a HOBO MX1102A CO_2 logger to control for any spike in atmospheric CO_2 and/or temperature. The pCO_2 logger was automatically calibrated to 400 ppm (as per manufacturer recommendations) by placing the logger in open air until a stable reading was recorded. This calibration did not permit accurate pCO_2 measurement but allowed to monitor fluctuations in pCO_2 during the experiments. Overall, atmospheric pCO_2 (437.7 ±34.6 ppm) varied by less than 10% throughout the experiment, and the mean temperature was recorded at 24.6 ±1.4 ºC (later rounded to 25 ºC for further processing). To compensate for such atmospheric pCO_2 measurement uncertainty, the estimated pCO_2 from the control batches was therefore used as the background concentration. Sample pCO_2 and Ω_A were calculated in CO2SYS using measured TA, DIC, salinity and temperature, with the K1 and K2 dissociation constants from Schockman and Byrne (2021), KSO_4 dissociation constant from Dickson (1990), KF dissociation constant from Perez and Fraga (1987) and the borate-to-salinity ratio from Lee et al. (2010).

For microscopic analysis, the dried Whatman filters were mounted on an aluminium holder using double-sided carbon sticky tabs. Scanning electron microscopy (SEM) analyses were conducted on a Hitachi TM4000 II tabletop SEM equipped with a Bruker QUANTAX energy-dispersive X-ray spectroscopy system (EDS). The second set of filters stored in Suprapure nitric acid was used to determine the concentrations of solid Ca and Mg, to assess whether $CaCO_3$ precipitated on undissolved $Mg(OH)_2$ particles. Analyses were performed using flame atomic absorption spectroscopy (F-AAS) on a Thermo Fisher Solaar S Series.

Changes in DIC attributed to CO_2 ingassing were used to derive the gas-transfer velocities and equivalent open-ocean wind speeds in each of the experiments. The DIC fluxes were estimated from the net changes in DIC between the control and the amended bottles. The change in DIC per day was estimated and inserted into the CO_2 flux equation from Wanninkhof (2014):

$$F = kK_0(pCO_{2w} - pCO_{2a}) \quad (1)$$

where F is the flux of CO_2 between the atmosphere and the seawater, K_0 is the solubility of CO_2 in seawater (obtained from Weiss, 1974, at 24.6 ºC and salinity of 35.346), and pCO_{2w} and pCO_{2a} are the partial pressures of the seawater and air in atm, respectively. This equation, combined with the water depth on the sampling day, was solved to calculate the gas velocity terms $k_{0\ RPM}$ and $k_{125\ RPM}$ in cm h^{-1}, for the 0 RPM and 125 RPM experiments, respectively. Finally, these gas-transfer velocities can be correlated to open-ocean wind speed using the gas exchange wind speed relationship from Wanninkhof (2014):

$$k = 0.251\ U^2 \left(\frac{Sc}{660}\right)^{-0.5} \tag{2}$$

where U^2 is the squared wind speed in m s^{-1}, and Sc is the Schmidt number at the measured temperature and salinity (Wanninkhof, 2014).

Statistical tests and TA budget

Throughout the experiment, laboratory conditions occasionally affected the performance of the DIC analyser. Therefore, measured DIC concentrations were routinely compared with DIC concentrations calculated independently from measured TA and pH_T measurements using CO2SYS. Because no changes in TA or pH_T accompanied randomly observed shifts in measured DIC, these deviations were attributed to analytical drift rather than changes in carbonate chemistry. For sampling campaigns showing systematic offset between measured and calculated DIC, measured DIC values were corrected using the mean ratio of all calculated to measured DIC values.

Changes in pCO_2 over time were analysed separately for the 0 and 125 RPM treatments using linear mixed-effects models implemented in MATLAB (MathWorks). The fixed effects included treatment, i.e., ΔTA targets, sampling time, and their interaction, while bottle identity was set as a random intercept to account for repeated measurements from the same experimental unit. Sampling time was treated as a categorical factor to avoid assuming a linear temporal response and to enable comparison among individual sampling dates. The control treatment and day 0 were specified as the reference levels for treatment and sampling time, respectively. Overall effects of treatment, sampling time, and their interaction were assessed using F-tests with Satterthwaite's approximation for the denominator degrees of freedom. Upon significant interaction between treatment and sampling time, planned one-sided post hoc contrasts were performed to compare each treatment with the control at each sampling time, testing the hypothesis that treatment pCO_2 was lower than that of the corresponding control. To account for multiple comparisons between treatments and the control at each sampling time, the one-sided p-values were adjusted using the Holm procedure. Treatment pCO_2 was considered significantly lower than the control when the estimated difference between treatment and control was negative and the corresponding one-sided adjusted p-value was < 0.05. Model assumptions were evaluated by visual inspection of residual-versus-fitted plots and normal probability plots of the residuals.

A TA generation efficiency metric was calculated by dividing the measured ΔTA after 24 hours by the targeted ΔTA. This $\%TA_{realised}$ can be used to compare the dissolution efficiency of the minerals based on the treatment. ~~After six~~

~~months~~Furthermore, a TA budget was derived from the carbonate chemistry measurements and mineral analyses at the end of the experiment. Measured TA loss (Meas. TA_{loss}) was calculated as the difference between the TA value at day 0 and the lowest measured TA value. Similarly, a theoretical maximum ΔTA (Max. ΔTA_{theo}) term was calculated using the mineral molar mass and the amount of material added in mg L^{-1} (assuming complete dissolution). From both estimates, a maximum TA_{loss} term (Max. TA_{loss}) was calculated from the difference between the Max. ΔTA_{theo} and the lowest recorded ΔTA. An estimate of particulate Ca concentration was derived from Max. TA_{loss} with each mole of TA loss corresponding to 0.5 mol $CaCO_3$.

Results

Differences between expected and measured alkalinity using solid feedstocks

Alkalinity additions for each experiment were performed identically with the two solid feedstocks, with ΔTA targets varying from +100 to +600 µmol kg^{-1}. In all experiments, the expected maximum ΔTA was not reached, but positive ΔTA values were observed at day 1 (Fig. 2). Stark differences emerged in realised TA based on the material used and the advection regime within the first 24 hours. ~~The $\%TA_{realised}$ values were significantly lower in bottles without advection (Fig. 2).~~ In the advected bottles, TA generation was higher, with $\%TA_{realised}$ values that were 2.5 ±1.0 and 4.3 ±2.1 times those in the static treatments for $Ca(OH)_2$ and $Mg(OH)_2$, respectively. For example, in the advected bottles with a ΔTA target of +100 µmol kg^{-1}, TA increased by 55-58 µmol kg^{-1} with $Ca(OH)_2$ and $Mg(OH)_2$, respectively, corresponding to $\%TA_{realised}$ values of 55-58%. However, TA generation in static bottles with a ΔTA target of +600 µmol kg^{-1} only yielded TA increases of 20-45 µmol kg^{-1} with $Ca(OH)_2$ and $Mg(OH)_2$, respectively, corresponding to $\%TA_{realised}$ values ranging from 3 to 8% (Figs. 2 and 3).

In all cases, the $\%TA_{realised}$ decreased with increasing ΔTA targets. Using $Mg(OH)_2$, the $\%TA_{realised}$ consistently decreased regardless of the advection speed, while using $Ca(OH)_2$, $\%TA_{realised}$ quickly decreased with advection and led to converging values for the 0 and 125 RPM regimes at ΔTA targets of 500 and 600 µmol kg^{-1}. TA generation from $Mg(OH)_2$ was generally lower than that from $Ca(OH)_2$, with values varying between 3-18% with $Mg(OH)_2$, and from 3 to 30% with $Ca(OH)_2$ relative to the expected TA increase. However, when exposed to advection, the TA generation of $Mg(OH)_2$ was mostly higher than when using $Ca(OH)_2$, and the decrease in efficiency was less pronounced than for $Ca(OH)_2$. Advection led to a $\%TA_{realised}$ varying from 10 to 55% using $Ca(OH)_2$, and from 29 to 58% using $Mg(OH)_2$.

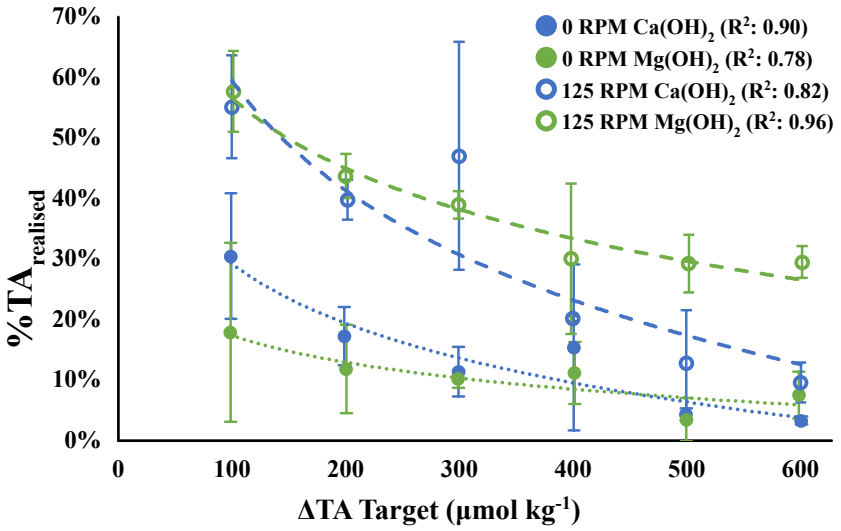

Figure 2: %TA$_{realised}$ from measured ΔTA after one day, as a function of the ΔTA target (in µmol kg^{-1}). Blue markers represent the Ca(OH)$_2$ treatments and green markers represent the Mg(OH)$_2$ treatments. Dotted lines represent logarithmic fits of the 0 RPM treatments while the dashed lines represent the logarithmic fits of the 125 RPM treatments. Corresponding R^2 values are provided in the legend. Each point represents the mean of the triplicate measurements, with error bars representing the uncertainty based on the standard deviation of these three measurements.

Long-term stability of alkalinity

In most cases, TA measured at 24 h was higher than measurements obtained during the remainder of the six-month experiment (Fig. 3). Two clear patterns emerged between the 0 RPM and 125 RPM incubations ~~(Fig. 3)~~. The absence of advection mostly led to a negative ΔTA over time. With Ca(OH)$_2$, clear TA losses followed the 500 and 600 µmol kg^{-1} additions, for which, after approximately two months, about 100 ±12 and 190 ±37 µmol kg^{-1} were lost, respectively. However, smaller additions led to slight changes in ΔTA but without a clear gain or loss over time. Using Mg(OH)$_2$ led to a clear decrease in alkalinity over time, with alkalinity loss increasing with the amount of material added. After a month, the two largest additions led to a loss in TA of 150-180 µmol kg^{-1}. The two medium additions led to a loss in TA of about 50 µmol kg^{-1}, while lower additions led to losses around 10-20 µmol kg^{-1}.

However, once exposed to advection, ΔTA remained positive in nearly all cases, except for the 600 µmol kg^{-1} addition with Ca(OH)$_2$. When targeting ΔTA of 100, 200 and 300 µmol kg^{-1} with Ca(OH)$_2$, ΔTA increased by ~50, ~80, and ~130 µmol kg^{-1} respectively, and remained relatively stable over time. The 400 and 500 µmol kg^{-1} additions did not generate more TA than the lower additions. Instead, their ΔTA values decreased over time, from ~80 to 40 µmol kg^{-1} for the 400 µmol kg^{-1} target, and from ~60 to about -5 µmol kg^{-1} for the 500 µmol kg^{-1}. Finally, the 600 µmol kg^{-1} treatment led to the lowest ΔTA increase of about 50 µmol kg^{-1} before decreasing steadily over six months down to about -140 µmol kg^{-1}. Conversely, the Mg(OH)$_2$ treatments led to increasing ΔTA with increasing additions, and positive values over the six-month experiment. The +100,

+200 and +300 µmol kg^{-1} treatments saw an increase over time in ΔTA despite a rather stable phase over the first week. The +400 and +500 µmol kg^{-1} treatments did not lead to a secondary increase in alkalinity but remained stable over the six-month experiment, following a peak in ΔTA on day 1 and slight loss until day 3. Finally, the highest $Mg(OH)_2$ treatment saw the greatest decrease in ΔTA over time, from nearly 180 µmol kg^{-1} on day 1 to 99 ±7 µmol kg^{-1} after two months, after which it remained stable until the end of the experiment.

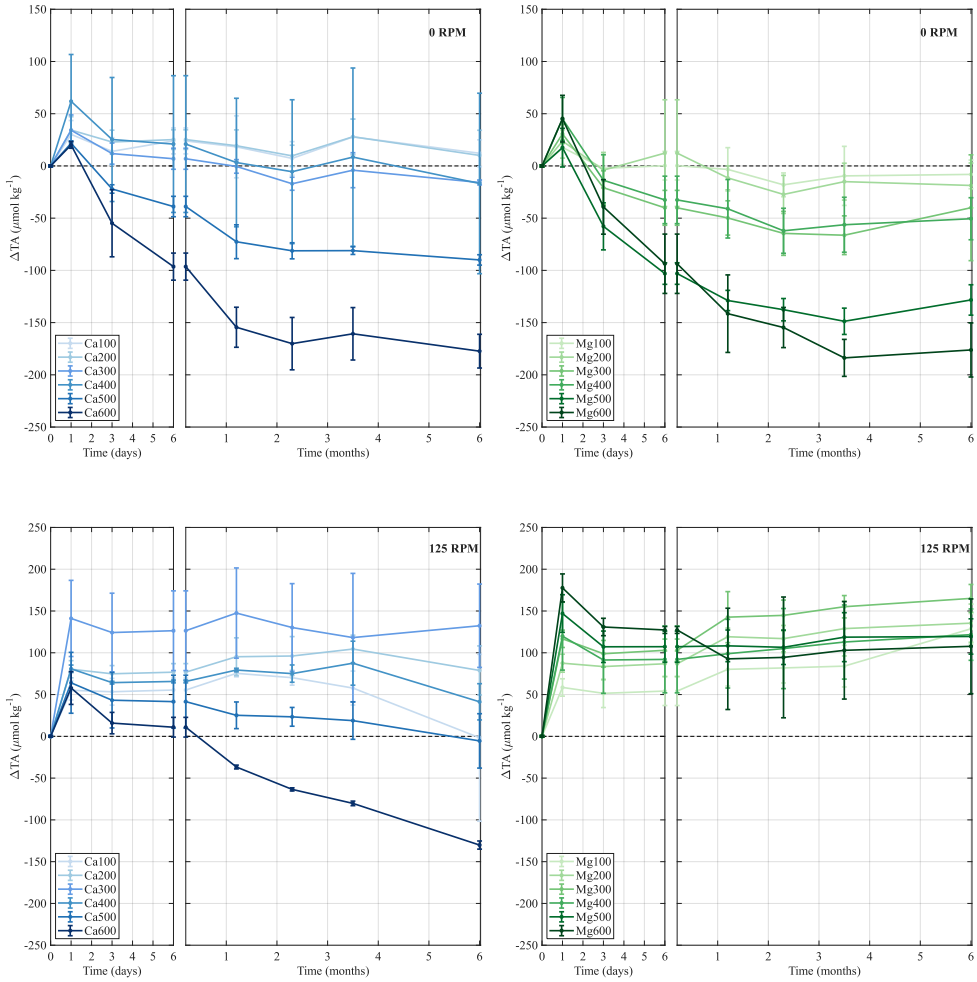

Figure 3: Changes in TA (ΔTA) as a function of time and expressed in µmol kg^{-1}, calculated by subtracting the same-day control TA from measured TA (the controls are represented by the black dotted line). The 0 RPM experiments are represented in the top two tiles, while the 125 RPM experiments are represented in the bottom two tiles. $Ca(OH)_2$ additions are represented in blue and $Mg(OH)_2$ additions in green, with the shades representing the amount added, i.e., the darker the shade, the larger the alkaline-material addition. Each point represents the average of triplicates, with error bars representing the uncertainty based on the standard deviation of these three measurements.

Effects of advection on pCO_2 changes

Following alkalinity additions, clear drops in the seawater pCO_2 were observed in all experiments (Fig. 4). In most cases, the decrease in pCO_2 was correlated with the target ΔTA, i.e., higher targeted ΔTA led to lower pCO_2. This was the case in most treatments except for the 0 RPM $Ca(OH)_2$ experiment, where the lowest pCO_2 was observed in the +400 µmol kg^{-1} experiment. In the 0 RPM experiments, the lowest pCO_2 recorded was 250-280 µatm in the $Ca(OH)_2$ and $Mg(OH)_2$ experiments~~, respectively~~. With both $Ca(OH)_2$ and $Mg(OH)_2$, pCO_2 slowly increased over one month but remained statistically significantly lower than the control pCO_2 values until day 3 on average in the $Ca(OH)_2$ treatments, and until day 6 on average in the $Mg(OH)_2$ and NaOH treatments (Fig. 7). Between days 6 and 35, the difference was no longer statistically significant (95% confidence, Table A2). Over the following four months, pCO_2 slightly varied, but followed fluctuations in the control bottles. In the 125 RPM experiment, the sharp drop in pCO_2 after alkaline material addition was followed by a sharp increase over the next days. In the case of $Ca(OH)_2$, the pCO_2 values were no longer significantly lower than those of the control incubations after only 72 h. The $Mg(OH)_2$ incubations' pCO_2 also quickly increased, becoming no longer significantly lower than the control pCO_2 on day 3 for additions of 100 and 200 µmol kg^{-1}, and on day 6 for additions of 300-600 µmol kg^{-1}. In both cases, the pCO_2 remained relatively stable over the following six months, with variations following the same patterns as for the control incubations.

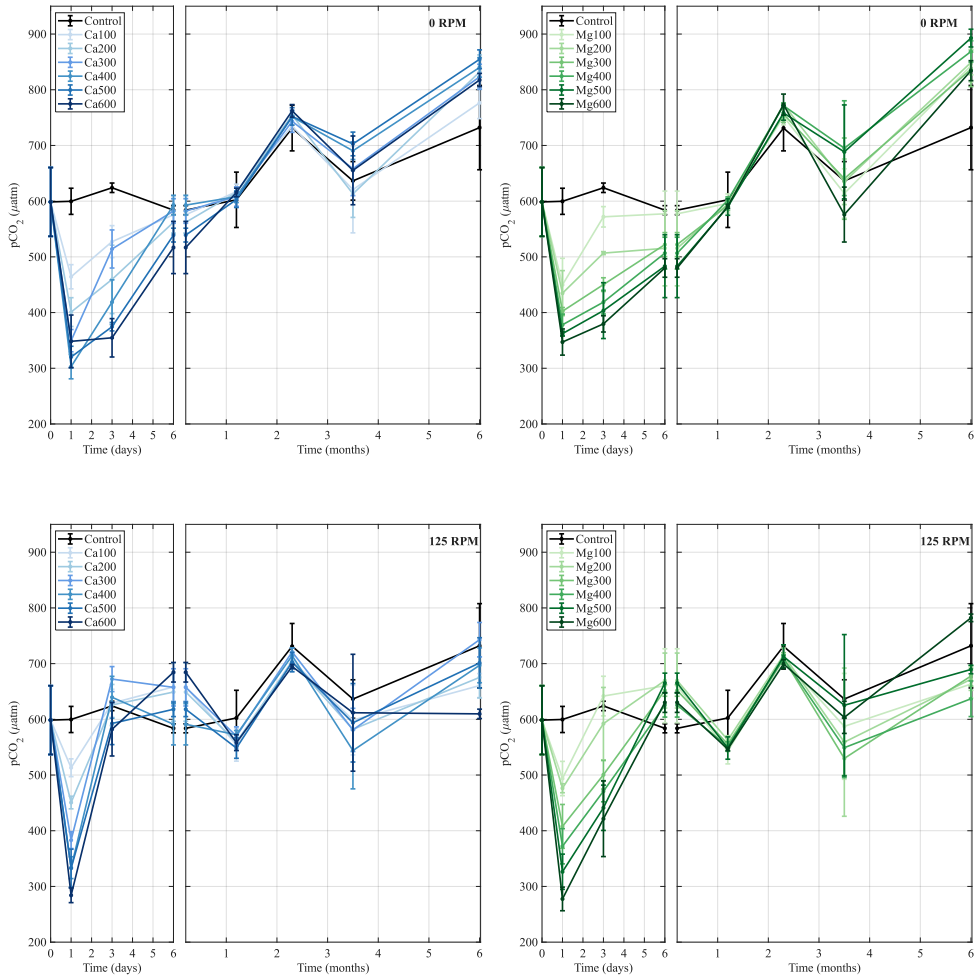

Figure 4: Estimated pCO_2 values from measured TA and DIC and reported in µatm, as a function of time. The 0 RPM experiments are represented in the top two tiles, while the 125 RPM experiments are represented in the bottom two tiles. $Ca(OH)_2$ additions are represented in blue and $Mg(OH)_2$ additions in green, with the shades representing the amount added, i.e., the darker the shade, the higher alkaline material addition. Each point represents the mean of the triplicate measurements, with error bars representing the uncertainty based on the standard deviation of these three measurements.

Calculated versus measured DIC

Throughout the experiment, DIC concentrations were measured directly and calculated from TA and pH_T measurements, as described in the "Material and methods" section. The ratio of calculated to measured DIC was determined for each sampling time point and is presented as individual boxplots, together with the combined dataset (Fig. 5). The boxplot analysis showed that the month 1 and 2 datasets had lower DIC ratios than the combined dataset, with mean ratios of 0.896 and 0.922, respectively, both below the lower quartile of the combined dataset (0.928). In contrast, the month 6 dataset exhibited higher

DIC ratios, with a mean of 0.969, exceeding the upper quartile of the combined dataset (0.957). In accordance with the criterion described in the "Material and methods" section, DIC concentrations for the month 1, 2, and 6 datasets were corrected using the average ratio derived from all measurements. Measured DIC values in the month 1 and 2 datasets were higher by ~101 ±5 µmol kg^{-1} and ~47 ±3 µmol kg^{-1} respectively, while the month 6 values were lower by ~67 ±4 µmol kg^{-1}.

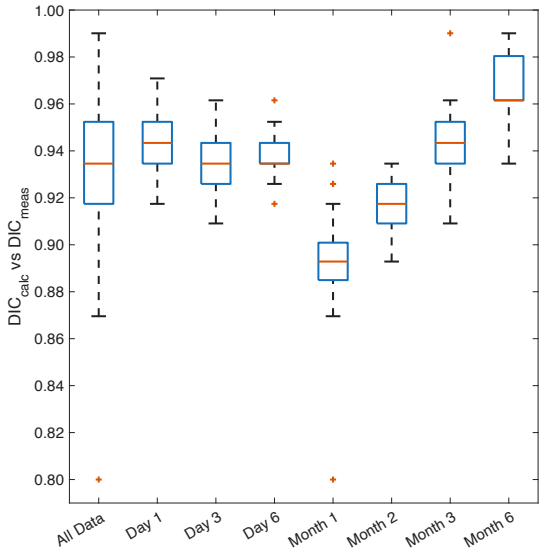

Figure 5: Boxplots of the ratio of DIC calculated from TA and pH_T measurements to measured DIC for the combined dataset and each sampling campaign. Ratios for the month 1 and 2 datasets fall below the ratio for the combined dataset, while the ratio for the month 6 dataset stands above.

CO_2 fluxes and derivation of equivalent wind speeds from DIC measurements

In almost all treatments, a decrease in DIC within the first 24 h was observed, followed by an increase in some cases. A decrease between days 1 and 3 was observed in the 0 RPM treatments and was particularly visible in the $Ca(OH)_2$ treatment with the highest target addition, i.e., ΔTA target of 600 µmol kg^{-1}, and in all $Mg(OH)_2$ treatments with ΔTA targets higher than 200 µmol kg^{-1}. Between days 1 and 3, rates of DIC change were -4.7 ±21.2 and 38.2 ±25.3 µmol kg^{-1} d^{-1} for the 0 and 125 RPM experiments, respectively. Using these rates of DIC change, Eq. (1) was solved, taking into account that the water depth in the bottle was ~10.5 cm at the time. For an average temperature of 24.6 ºC and salinity of 35.4, K_0 is approximated to 2.932 x 10^{-2} mol L^{-1} atm^{-1} as per Weiss (1974). The differences between pCO_{2w} and pCO_{2a} were derived from Fig. 6 and averaged to 221.6 ±71.2 and 256.5 ±96.8 µatm for the 0 and 125 RPM treatments, respectively. Solving Eq. (1) for a bottle with an internal diameter of 9.6 cm yielded a $k_{0\ RPM}$ and $k_{125\ RPM}$ values of 0.4 ±0.7 and 2.5 ±1.0 cm h^{-1}, respectively. Solving the second

equation with a Schmidt number Sc of ~533.2 at 24.6 ºC and salinity 35.4 (Wanninkhof, 2014) yielded corresponding U wind speeds of 1.2 ±1.4 and 3.0 ±2.5 m s^{-1}.

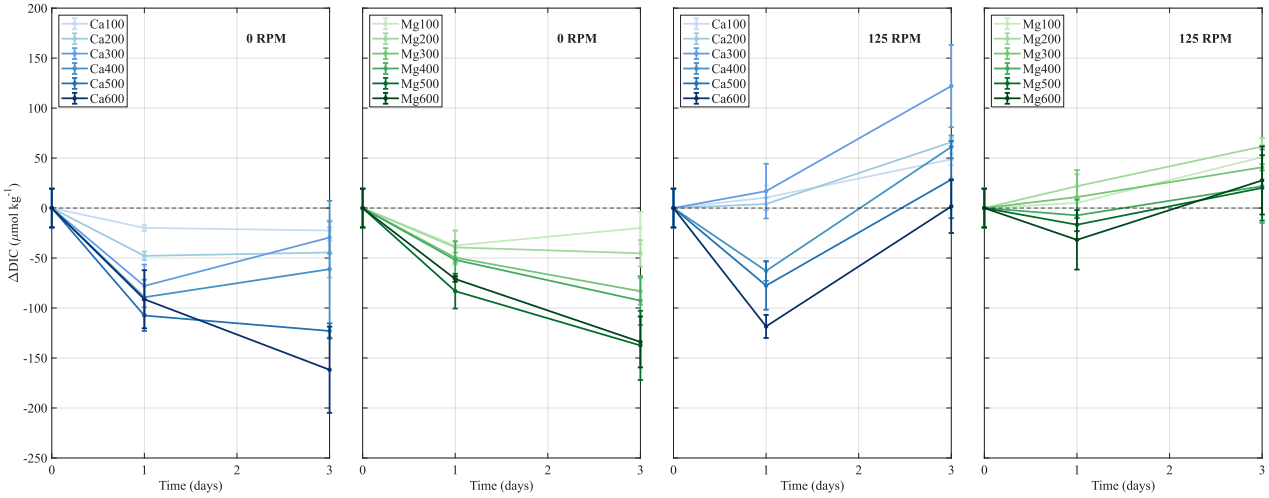

Figure 6: Changes in DIC within the first three days after $Ca(OH)_2$ (blue) or $Mg(OH)_2$ (green) additions with 0 RPM (two left-hand panels) and 125 RPM advection (two right-hand panels). The darker shades indicate higher alkaline material additions. Each point represents the mean of the triplicate measurements, with error bars representing the uncertainty based on the standard deviation of these three measurements.

NaOH experiments and differing patterns

NaOH additions were performed identically in static and advected bottles. However, a clear difference in ΔTA emerged between the two advection regimes. At 0 RPM, ΔTA only reached about 278 µmol kg^{-1} within 24 h and peaked at 337 µmol kg^{-1} after three days, corresponding to about 56% of the expected TA (Fig. 7). The 125 RPM experiments quickly reached about 552 µmol kg^{-1} after one day, before reaching up to 598 µmol kg^{-1} after three months, corresponding to about 100% of the expected TA increase (within measurement uncertainty). DIC followed a similar pattern in both cases, but the final ΔDIC was approximately half as large in the 0 RPM treatment as in the 125 RPM treatment. Also, while ΔDIC was positive throughout the experiment at 125 RPM, the 0 RPM experiment first showed a decline on day 1 of about 17 µmol kg^{-1} before consistently increasing until the end of the experiment. pCO_2 decreased after NaOH addition down to similar levels for both 0 and 125 RPM experiments, i.e., 209 and 167 µatm, respectively. The increase that followed was quicker in the 125 RPM experiments, where, after only six days, pCO_2 was no longer significantly lower than the control, while it took at least one month for pCO_2 to be similar to the 0 RPM control (Table A2).

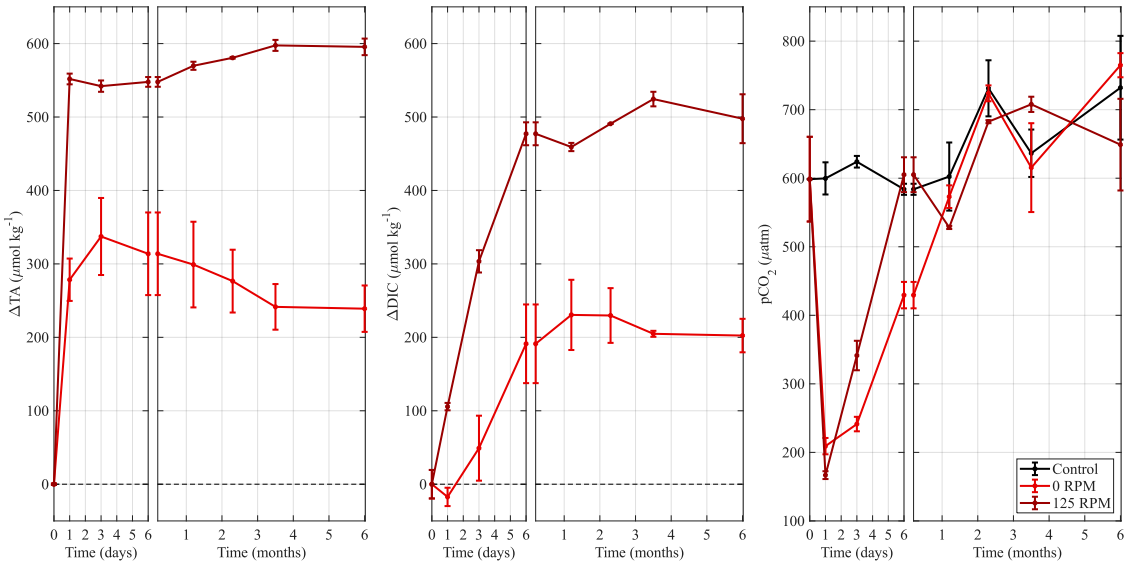

Figure 7: ΔTA, ΔDIC and pCO_2 changes as a function of time for the NaOH experiments. The black colour represents the control experiment, the lighter red colour represents the 0 RPM experiments, and the darker red colour represents the 125 RPM experiments. Each point represents the mean of the triplicate measurements, with error bars representing the uncertainty based on the standard deviation of these three measurements.

TA loss budget, particulate analysis and scanning electron microscopy

Particulate analysis was conducted using the precipitates from the highest $Mg(OH)_2$ addition, i.e., +600 µmol kg^{-1}, at both 0 and 125 RPM, to provide sufficient material to determine whether $CaCO_3$ precipitated onto $Mg(OH)_2$ particles. The Max. TA_{loss} values for the 0 RPM treatment were higher than those for the 125 RPM by about 194 µmol kg^{-1} (Table 2). The results obtained from F-AAS revealed higher Ca^{2+} and Mg^{2+} concentrations in the 0 RPM treatments, with values about 7.2 and 0.4 mg L^{-1} higher, respectively. On average, 62.7% ±4.4% and 58.2% ±5.2% of the estimated particulate Ca was accounted for by the measured Ca^{2+}, in the 0 and 125 RPM treatments, respectively. Finally, another major difference emerged from the measurements of Mg^{2+}, where the 0 RPM treatment yielded nearly twice as much particulate Mg as in the 125 RPM treatment. Overall, the particles collected from the 0 RPM experiments contained 3.8% ±0.4% Mg^{2+}, while the particles collected from the 125 RPM experiments were about 3.0% ±0.3% Mg^{2+}.

Table 2: Comparison of theoretical and measured TA changes and particulate Ca and Mg concentrations in the 0 and 125 RPM $Mg(OH)_2$ treatments with a target ΔTA of +600 µmol kg^{-1}. The table includes the theoretical maximum ΔTA assuming complete dissolution, measured and maximum TA losses, Ca^{2+} concentrations estimated from TA loss, measured Ca^{2+} and Mg^{2+}

concentrations, and the ratio of measured to estimated Ca^{2+}. The third replicate of the 0 RPM treatment was lost during analysis. Hence, not all values could be calculated for this sample.

Sample replicate		Max. ΔTA_{theo} (µmol kg^{-1})	Meas. TA_{loss} (µmol kg^{-1})	Max. TA_{loss} (µmol kg^{-1})	Estimated Ca^{2+} (mg L^{-1})	Measured Ca^{2+} | Mg^{2+} (mg L^{-1})	Measured/ estimated (%)
0 RPM	1	596.6	172.6	769.1	38.5	25.3 | 1.1	65.8%
	2	601.5	199.6	801.1	40.1	23.9 | 0.9	59.6%
	3	598.1	216.4	814.5	40.7	LOST	LOST
125 RPM	1	605.2	-6.0	599.2	30.0	16.8 | 0.5	56.1%
	2	598.8	66.7	665.5	33.3	18.1 | 0.5	54.4%
	3	600.6	-62.9	537.7	26.9	17.2 | 0.6	64.1%

From the same incubations, as well as from the highest $Ca(OH)_2$ addition experiments at 0 and 125 RPM, samples for SEM analysis were taken and analysed. Precipitate analyses revealed clear and strong signals for calcium, oxygen and carbon in all samples, with traces of magnesium, strontium, sodium and chloride, i.e., <1% on average compared to the above-mentioned elements. While no clear difference in the composition of precipitates was observed, the morphology was clearly different. Precipitates from the $Ca(OH)_2$ experiments were all needle-like, as shown in Fig. 8. A major difference emerged between these precipitates and those from the $Mg(OH)_2$ experiments. In the $Mg(OH)_2$ treatments, the morphology of the crystals was clearly different, with crystals appearing denser and displaying a broccoli-like structure. Although individual crystals were more difficult to distinguish, these precipitates were generally larger than those observed in the $Ca(OH)_2$ experiments (Fig. 8).

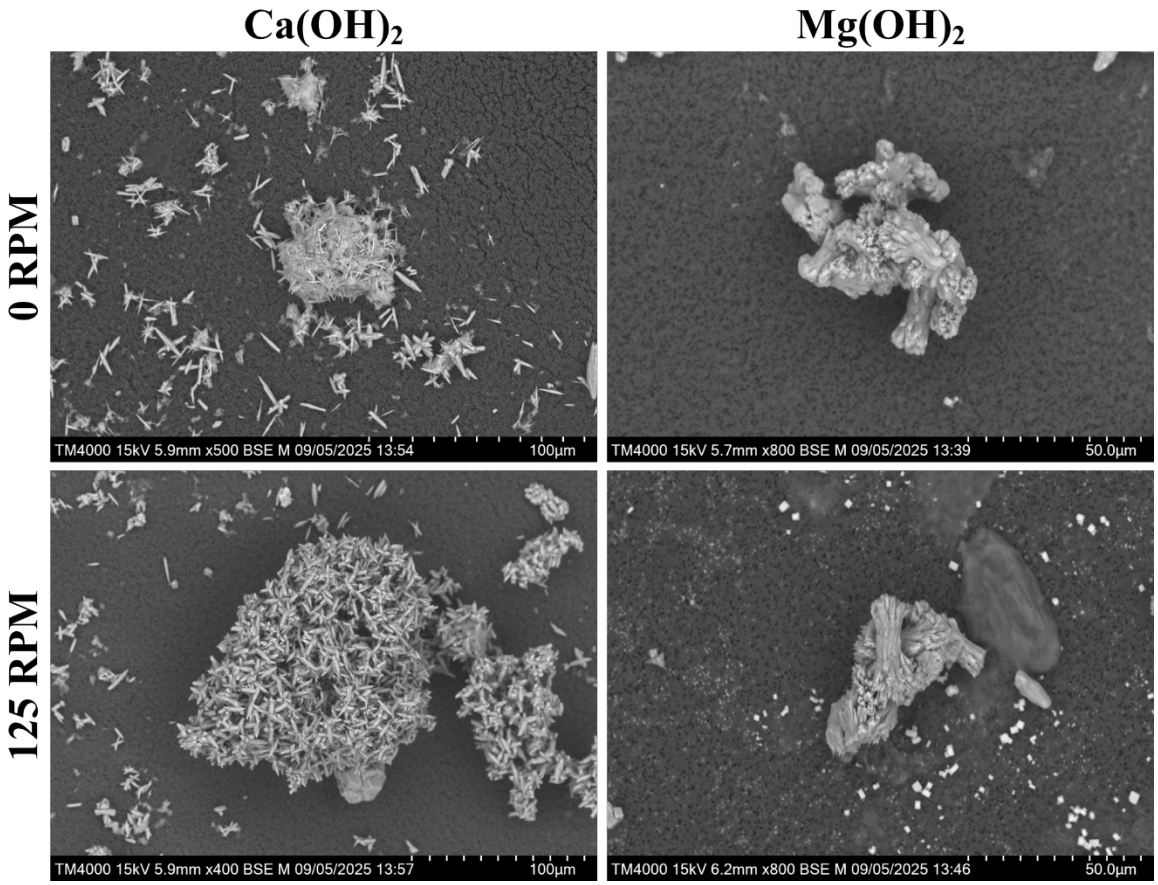

Figure 8: SEM images of precipitates collected from the ΔTA +600 µmol kg^{-1} experiments amended with $Ca(OH)_2$ (left) and $Mg(OH)_2$ (right), both at 0 RPM (top) and 125 RPM (bottom).

Discussion

Advection affects alkaline material dissolution, $CaCO_3$ precipitation, and CO_2 ingassing rates

The results indicate that hydrodynamics influence several physicochemical processes in parallel, affecting mineral dissolution, carbonate chemistry, secondary precipitation and realised CDR. A first clear outcome is that the alkalinity generated through $Ca(OH)_2$ and $Mg(OH)_2$ dissolution using a shaking table was substantially lower than reported in the literature (Hartmann et al., 2023; Moras et al., 2022; Moras et al., 2024; Varliero et al., 2024; Yang et al., 2023). Such an outcome was expected as the weaker turbulence generated by the shaking table compared with that produced by a stir bar, for example, could have decreased fluid exchange around the dissolving particles and enhanced their settling. Consequently, the dissolution was likely limited by mass transfer through the diffusive boundary layer surrounding particles (Lasaga, 2014; Levich, 1962; Saez Moreno

et al., 2026; Sulpis et al., 2019). The reduced advection could have increased the thickness of the diffusive boundary layer surrounding particles, reducing the diffusive flux of dissolved products away from the particles surface. This in turn could have ~~leading~~ created~~to~~ micro-environments enriched in Ca^{2+}, Mg^{2+} and OH^-~~.~~, ~~These could have reduced the concentration gradient driving diffusion~~increasing local saturation state and ultimately decreased dissolution rates. In our case, the low (125 RPM, Reynolds number of ~1.7 x 10^4) or absent (0 RPM) turbulence coincided with a decrease in TA generation efficiency and suggest mass-transfer limitations (Drever, 1997; Saez Moreno et al., 2026). At 0 RPM, TA generation was consistently lower ~~up to 50% lower for the lower additions~~in static conditions compared to the advected conditions. At the same time, the persistence of such concentrated micro-environments increased the risk of heterogeneous and pseudo-homogeneous $CaCO_3$ precipitation (Marion et al., 2009). The competing processes of reduced dissolution and increased $CaCO_3$ precipitation likely explain the substantially lower measured alkalinity increase, at most half of reported values in literature, especially in the 0 RPM incubations. Although we did not directly measure such chemical gradients and micro-environments, the dissolution and precipitation patterns are consistent with the behaviour expected from thicker diffusive boundary layers surrounding dissolving particles (Lasaga, 2014; Levich, 1962). Taken together, these findings and previous studies using hydroxide and olivine-rich feedstocks suggest that hydrodynamic conditions are a first-order control on realised alkalinity generation (Flipkens et al., 2023; Fuhr et al., 2025; Meysman and Montserrat, 2017). Expected alkalinity generation should therefore not be simply inferred from the alkaline material properties but rather a combined result of material properties and surrounding hydrodynamic regime. Environments with strong advection and/or physical disturbance, such as strong porewater exchange or water flow generating high bed shear stress, may therefore be more suitable, as previously suggested for olivine-rich materials (Flipkens et al., 2023; Meysman and Montserrat, 2017).

A similar influence of advection was also observed in the NaOH treatments, in which the two advection regimes produced noticeably different TA increases. Under advected conditions, TA reached about 92% of the expected TA within one day before consistently increasing to reach 100% on day 108 (Fig. 7). The initially reduced TA generation was not accompanied by a decrease in DIC, suggesting that $CaCO_3$ formation was unlikely to be the source of the missing TA. Similar patterns were observed in the literature and attributed to $Mg(OH)_2$ formation following NaOH addition, both experimentally at pH above ~10 (Haas, 1916; Kapp, 1928) and in the context of OAE (Hashim et al., 2025; Shaw et al., 2025; Suitner et al., 2024; Varliero et al., 2024). The progressive increase in TA to 100% after three months is consistent with gradual dissolution of temporarily precipitated $Mg(OH)_2$ (Haas, 1916; Hashim et al., 2025; Kapp, 1928). Secondary mineral formation has recently been considered a loss in TA efficiency for OAE (Lunstrum et al., 2026). However, this transient $Mg(OH)_2$ formation may represent a temporary reduction in alkalinity generation rather than a permanent loss of CDR potential. A contrasting pattern was observed in the static NaOH-amended bottles. There, the maximum TA generated only reached about 55% on day 3 before decreasing further. The concomitant decrease in TA and DIC suggests that $CaCO_3$ precipitation after NaOH addition became the dominant process, likely obscuring the signal of subsequent $Mg(OH)_2$ dissolution (Fig. 7).

Advection also directly affected CO_2 ingassing rates. In the advected bottles, pCO_2 was no longer significantly lower than the control within three days in most treatments, and at most within six days for the higher treatments using $Mg(OH)_2$ and NaOH.

Without advection, the differences in pCO_2 between amended bottles and controls remained statistically different for at least six days, and up to 35 days in some instances. The faster ingassing rapidly increased DIC, which in turn rapidly reduced carbonate supersaturation (Zeebe and Wolf-Gladrow, 2001). This buffering likely decreased the risk of $CaCO_3$ precipitation. Together, these observations indicate that hydrodynamic conditions strongly influence dissolution kinetics, atmospheric CO_2 ingassing rates and secondary mineral formation, and therefore the alkalinity generation efficiency of OAE.

CO_2 invasion and alkaline feedstock influence $CaCO_3$ precipitation patterns and morphologies

Although $CaCO_3$ precipitation occurred in nearly all solid-amended bottles, its pattern and temporal evolution differed between advected and static bottles. $CaCO_3$ formation in the context of OAE has been described as a runaway process when using such feedstocks, in which the amount of alkalinity removed from the system accelerates over time and may become higher than the amount of alkalinity added (Hashim et al., 2025; Moras et al., 2022; Moras et al., 2024; Suitner et al., 2026). Here, such behaviour was observed in most of the 0 RPM experiments. However, the pattern of alkalinity loss attributed to $CaCO_3$ precipitation in the 125 RPM treatments differed. A seemingly linear and constant loss was observed in the $Ca(OH)_2$ experiments with a target ΔTA of +600 µmol kg^{-1}, whereas in the other 125 RPM treatments, the early loss attributed to $CaCO_3$ formation quickly stopped after a few days of incubation. To our knowledge, these patterns have not been reported in the literature for hydroxide-based OAE application before this study or the recent preprint by Saez Moreno et al. (2026).

The decrease and halt in the precipitation process coincided with CO_2 invasion. Under advected conditions, CO_2 invasion occurred more rapidly. When CO_2 dissolves in water, it reacts with a carbonate ion, CO_3^{2-}, to form two bicarbonate ions, HCO_3^- (Zeebe and Wolf-Gladrow, 2001). This consumption of CO_3^{2-} decreases Ω_A, which directly influences $CaCO_3$ formation rates (Suitner et al., 2026). These observations suggest that rapid CO_2 ingassing may have reduced the risk of runaway $CaCO_3$ precipitation. Consequently, more rapid CO_2 ingassing likely shortened the CAP, reducing or, in some cases, preventing runaway precipitation. Conversely, slower CO_2 ingassing in the 0 RPM experiments was associated with a longer CAP and runaway $CaCO_3$ precipitation (Fig. 4). Hence, the risk of loss of TA through $CaCO_3$ precipitation appears to depend not only on the initial amount of alkalinity and form of alkalinity added, but also on the rate of CO_2 ingassing. These findings complement earlier studies showing that secondary $CaCO_3$ formation is influenced by mineral surface area, realised alkalinity, saturation state and precipitation inhibitors (Fuhr et al., 2022; Moras et al., 2022; Pan et al., 2021; Rigopoulos et al., 2018; Suitner et al., 2026). It also demonstrates that CO_2 invasion and hydrodynamic conditions regulate CAP duration and directly influence alkalinity generation.

The different rates of CO_2 ingassing resulted in a broader range of Ω_A at which precipitation stopped. Previous OAE experiments with similar materials reported that precipitation ceased at Ω_A ~2 (Hashim et al., 2025; Moras et al., 2022; Moras et al., 2024). In our experiments, the observed final Ω_A values were higher, particularly in the 125 RPM experiments, with values ranging between 2.2 and 3.6 (Fig. A2). This discrepancy most likely resulted from differences in experimental setups, particularly the fact that each bottle was open to the air. The continuous atmospheric CO_2 ingassing allowed in the system by the open-bottle design progressively reduced the $CaCO_3$ supersaturation. These observations suggest that OAE deployments

may benefit from settings in which physical and/or air-sea gas exchange rapidly reduce local supersaturation. In natural systems, physical dilution and hydrodynamics in general are expected to reduce local supersaturation on shorter timescales than atmospheric CO_2 equilibration alone. Atmospheric CO_2 invasion should therefore be considered together with physical transport processes. Such settings could include areas with relatively rapid atmospheric CO_2 invasion or horizontal dilution, provided that alkalised water remains near the surface long enough for atmospheric equilibration (Jones et al., 2014; Lunstrum et al., 2026; Zeebe and Wolf-Gladrow, 2001). In the absence of advection, however, particle settling was likely more important, which may have reduced dissolution, increased the diffusive boundary layer around the particles and increased high saturation micro-environment at the bottom of the bottles. The smaller gradient of pCO_2 between air and water, coupled to the decreased invasion rate also likely enhanced the persistence of the CAP. Therefore, the buffering by CO_2 ingassing but most importantly the larger diffusive boundary layer resulting from the absence of advection ~~and CO_2 invasion,~~ eventually ~~promoting $CaCO_3$ precipitation. Coupled to weaker CO_2 invasion, the absence of fluid exchange around particles could have maintained higher local concentrations of Ca^{2+} and possibly Mg^{2+} around particles,~~ lea~~d~~ing to further $CaCO_3$ precipitation and lower final Ω_A values, i.e., from 1.8 to 2.6.

SEM-EDS analyses were consistent with the formation of $CaCO_3$ and revealed differing morphologies depending on the alkaline material used (Fig. 8). All crystal morphotypes were morphologically consistent with previously reported aragonite precipitates formed in comparable seawater conditions, i.e., natural seawater at 25 ºC, while EDS analyses did not reveal significant incorporation of other measured elements (Morse et al., 1997). Precipitates in $Ca(OH)_2$-amended seawater consisted of needle-like $CaCO_3$ crystals morphologically consistent with aragonite crystals described in Moras et al. (2022). However, in $Mg(OH)_2$-amended seawater, precipitates formed spherulitic, broccoli-shaped $CaCO_3$ structures, morphologically consistent with aragonite synthesised by Suitner et al. (2024). Synthesis of aragonite has been undertaken in a variety of experimental setups, with morphology influenced by factors including Mg:Ca ratios and dissolved organic matter (Chave and Suess, 1970; Morse et al., 1997; Pan et al., 2021; Pytkowicz, 1965; Rushdi et al., 1992). Because all of our experiments were conducted in parallel using the same batch of seawater, differences in the starting Mg:Ca ratio or dissolved organic matter concentrations were negligible. Instead, the differences were more likely related to the alkaline feedstock used. The dissolution of $Mg(OH)_2$ may have resulted in higher concentrations of Mg^{2+} in the diffusive boundary layer of particles compared to $Ca(OH)_2$. The role of Mg in delaying and restricting $CaCO_3$ formation is well-documented in the literature (Morse et al., 1997; Pan et al., 2021; Pytkowicz, 1965). Prolonged exposure to Mg-rich micro-environments has previously been associated with slower aragonite formation, favouring broccoli-shaped over needle-like crystals. Although these micro-environments were not directly quantified here, these observations are consistent with previously reported heterogeneous precipitation occurring within micro-environments with differing chemical compositions (Beck and Andreassen, 2010; Gránásy et al., 2005; Tracy et al., 1998; Zubovic et al., 2025).

Altered CDR potential of $Ca(OH)_2$ and $Mg(OH)_2$ and implications for MRV

The observations reported above have direct implications for estimates of the realised CDR potential of OAE, as both incomplete mineral dissolution and secondary precipitation determine realised alkalinity and therefore the total CO_2 uptake potential. Atmospheric CO_2 invasion is a major determinant of OAE efficiency, particularly its realised CDR potential, although it depends strongly on the material used. $Ca(OH)_2$ and $Mg(OH)_2$ are among the most widely investigated feedstocks for OAE (Eisaman et al., 2023; Moras et al., 2022; Moras et al., 2024; Shaw et al., 2025; Varliero et al., 2024; Yang et al., 2023). Thermodynamically, both minerals generate two moles of alkalinity per mole of mineral dissolved, corresponding to a theoretical CDR potential of 0.9-1.1 $tCO_2\ t^{-1}$ $Ca(OH)_2$ and 1.1-1.4 $tCO_2\ t^{-1}$ $Mg(OH)_2$, assuming a CO_2 uptake efficiency of 0.75-0.9 moles of CO_2 captured per mole of TA (Schulz et al., 2023). This potential decreases drastically if, for example, the CO_2 emitted during the calcination of limestone to produce $Ca(OH)_2$ is not captured (Caserini et al., 2021; Foteinis et al., 2022; Kheshgi, 1995). Our results also point to an additional limitation, the incomplete TA generation. Under a conservative OAE deployment scenario, e.g., ΔTA +100 $\mu mol\ kg^{-1}$ (Bach et al., 2025), and moderate advection, e.g., 125 RPM, the realised TA only reached 55-58% (Fig. 2). The realised CDR potential of solid-based OAE therefore depends not only on the chemistry and quantity of material added, but also on hydrodynamic conditions, the fraction of TA realised, and the amount of atmospheric CO_2 ultimately taken up.

Although these processes are more readily quantified in a controlled laboratory setting, they become increasingly difficult to distinguish under open ocean conditions. In principle, incomplete dissolution can be differentiated from $CaCO_3$ precipitation by measuring both TA and DIC in the system. Limited TA generation without a DIC decrease may indicate incomplete dissolution, while a concomitant decrease in TA and DIC in an approximate 2:1 ΔTA:ΔDIC ratio may indicate $CaCO_3$ precipitation. Once CO_2 ingassing occurs, the resulting DIC increase hides this stoichiometric relationship, making the quantification of realised TA more difficult. This represents an important challenge for monitoring, reporting and verification (MRV) efforts during field-scale OAE deployments. Current MRV protocols recognise loss terms, such as biotic calcification, additionality and secondary mineral formation, but the distinction between incomplete dissolution and $CaCO_3$ precipitation becomes more difficult to constrain once atmospheric CO_2 ingassing alters DIC (Bach, 2024; Isometric, 2026; Lunstrum et al., 2026). To date, the first independently verified carbon credits generated from coastal OAE deployment were issued under the Isometric protocol to the Halifax-based company Planetary (Isometric, 2026; Kauk, 2025). The protocol requires monitoring of effluent characteristics, particularly pH, to ensure compliance with regulatory thresholds that must not be exceeded. In the United States, historical Environmental Protection Agency aquatic life criteria established an upper pH guideline of 8.5 and 9.0 for saltwater and freshwater ecosystems, respectively. However, the European Union does not prescribe a single pH limit for surface waters (European Parliament and Council of the European Union, 2000; U.S. Environmental Protection Agency, 1986, 2026). Our observations support the need for such a process-based approach and identify processes that should be considered in a future iteration of MRV protocols.

As mentioned earlier, current MRV protocols account for loss of TA to secondary mineral formation through a loss-term (Isometric, 2026). Hence, reliably quantifying secondary $CaCO_3$ precipitation remains one of the major uncertainties for OAE efficiency and MRV. Although precipitated $CaCO_3$ may contribute to long-term CDR, its formation in surface waters consumes alkalinity that would otherwise remain available for atmospheric CO_2 uptake, and therefore reduces the near-term CDR potential of OAE (Lunstrum et al., 2026; Moras et al., 2022). Although secondary $CaCO_3$ is unlikely to redissolve rapidly in natural open-ocean surface waters, it may settle onto coastal sediments or be exported to the deeper ocean, where it may later dissolve below the carbonate compensation depth or become buried in sediments where further dissolution may occur (Dale et al., 2024; Fuhr et al., 2023; Fuhr et al., 2024; Fuhr et al., 2025; Suitner et al., 2026). This temporary loss of CDR potential could become a second source of alkalinity overtime, though it is yet to be fully ~~addresses~~addressed. Nevertheless, because secondary $CaCO_3$ in our experiments mostly formed heterogeneously on added particles, export of coated undissolved feedstock could reduce further alkalinity generation within the surface layer, constituting an additional near-term loss in CDR potential.

The morphology of secondary $CaCO_3$ precipitates may also influence such transport. Based on modelling considerations from Suitner et al. (2026), the porous needle-like structures observed in the $Ca(OH)_2$-amended bottles are unlikely to inhibit dissolution because seawater can seep between the needle structures and reach undissolved particles. In contrast, the slower dissolution of $Mg(OH)_2$ seems to favour slow-growing, denser broccoli-shaped structures. The higher Ca^{2+} and Mg^{2+} concentrations measured in the precipitates from the 0 RPM experiments support the interpretation that $CaCO_3$ coated $Mg(OH)_2$ particles (Table 2). Such coatings could simultaneously reduce dissolution efficiency while increasing particle density and thereby promoting export of undissolved $Mg(OH)_2$ particles from the mixed layer. Conversely, rapid particle export could significantly decrease the surface area available for further precipitation, limiting the loss of TA to $CaCO_3$ (Baltruschat et al., 2026; Suitner et al., 2026).

Although highly relevant to OAE applications, such physical processes are poorly represented in bottle experiments. In natural systems, vertical and horizontal transport, tidal mixing and dilution would further reduce local supersaturation and available surface area for precipitation, as may occur in point-source alkalinity release (Lee et al., 2026). While this was not tested here, these processes could shorten the CAP duration more rapidly than atmospheric CO_2 ingassing alone because CO_2 equilibration occurs over longer timescales in the open ocean and varies substantially with latitude and season (Zhou et al., 2025). Better constraining these coupled physical and geochemical processes should therefore be a priority for future OAE research. Dedicated experiments incorporating realistic hydrodynamics, atmospheric CO_2 equilibration and particle transport would improve estimates of realised CDR and provide valuable constraints for future MRV protocols.

Implications of the CAP duration for CO_2 uptake and environmental impacts

A primary outcome of this research is the close coupling between the CAP duration and multiple geochemical processes. Hydrodynamics influenced mineral dissolution and CO_2 invasion, while $CaCO_3$ precipitation and CO_2 invasion affected carbonate chemistry and determined the duration of the CAP. During the first few days after alkalinity addition, DIC

measurements yielded estimated net CO_2 fluxes inferred from DIC changes of -4.7 ±21.2 and 38.2 ±25.3 µmol kg^{-1} d^{-1} for the 0 and 125 RPM experiments, respectively. However, these rates coincided with a decrease in TA during that time, most likely resulting from $CaCO_3$ formation, as indicated by the simultaneous decrease in TA and the negative apparent flux of CO_2 in the 0 RPM treatments. This simultaneous removal of DIC likely biased the inferred CO_2 fluxes. Estimated DIC loss to $CaCO_3$ can be inferred from TA loss, where for each mole of TA lost to $CaCO_3$, 0.5 mole of DIC is removed. This resulted in about 10.9 ±6.3 and 4.8 ±4.0 µmol kg^{-1} d^{-1} in the 0 and 125 RPM treatments respectively, corresponding to about 1.1 and 0.5 mg $CaCO_3$ kg^{-1} d^{-1}. Correcting for this loss substantially increased the estimated CO_2 fluxes, especially in the 0 RPM treatments, yielding 5.3 ±15.5 and 43.0 ±25.1 µmol kg^{-1} d^{-1} for the 0 and 125 RPM experiments, respectively. This supports the need to combine carbonate chemistry measurements with direct CO_2 flux estimates, because in field applications, such uncertainty could lead to underestimation of the realised CDR.

The corrected fluxes correspond to gas-transfer velocities $k_{0\ RPM}$ and $k_{125\ RPM}$ of 0.8 ±0.6 and 2.8 ±0.9 cm h^{-1}, respectively. These values are lower than typical mean open-ocean gas-transfer velocities, commonly averaging between 14 and 20 cm h^{-1}, though records range from nearly 0 to roughly 50 cm h^{-1}. Although derived from simplified laboratory experiments, these gas-transfer velocities provide a useful first-order approximation for comparison with empirical air-sea gas exchange parametrisations. The derived wind speeds should therefore be interpreted as gas-exchange equivalents rather than direct hydrodynamic analogues of open-ocean conditions (Frew et al., 2007; Yu et al., 2013; Zhou et al., 2023). Using the parametrisation of Wanninkhof (2014), corrected equivalent wind speeds were estimated to be 1.7 ±1.0 m s^{-1} and 3.1 ±0.7 m s^{-1}, respectively. Wind speeds in the open ocean vary greatly, from less than 1 m s^{-1} to over 20 m s^{-1} during heavy wind and storm periods, with a mean of approximately 6 m s^{-1} (Ho et al., 2006; Miller et al., 2010; Risien and Chelton, 2008). Hence, the data presented here provide a first-order approximation to gas transfer velocities associated with low to moderate wind scenarios and may provide useful constraints for modelling low-wind or weak gas-exchange conditions. Stronger winds may enhance wave-driven turbulence, in turn enhancing mineral dissolution and air-sea CO_2 exchange. However, their overall influence on the CAP duration will also mostly depend on mixed-layer deepening, dilution, and vertical transport, which will determine the residence time of alkalised water near the surface (Cushman-Roisin and Beckers, 2011; England and Bach, 2025; Flipkens et al., 2023; Tokinaga and Xie, 2011).

Although the present study did not focus on biological responses to OAE perturbations, the observed carbonate chemistry changes may provide a useful framework to interpret previously published OAE-focused laboratory and mesocosm research. Biological responses to OAE are generally expected to arise primarily from associated changes in carbonate chemistry, including increased pH and reduced dissolved CO_2 concentration, rather than from TA increase in isolation (Bach et al., 2019). Several studies have explored the impacts of OAE on a wide range of organisms, from single-species laboratory incubations to large-scale mesocosm campaigns encompassing natural phytoplankton communities and fish larvae (Faucher et al., 2025; Ferderer et al., 2022; Ferderer et al., 2024; Goldenberg et al., 2024; Kousoulas et al., 2025; Paul et al., 2025; Ramírez et al., 2025; Schneider et al., 2026). Experiments conducted using an equilibrated approach, i.e., a TA increase accompanied by a DIC increase, resulted in low to negligible pH and pCO_2 changes (Kousoulas et al., 2025; Paul et al., 2025; Ramírez et al.,

2025). Without depletion of the CO_2 concentration, biological responses were small to negligible in most cases. However, non-equilibrated approaches with materials such as $Ca(OH)_2$, $Mg(OH)_2$ and NaOH increased TA without an accompanying initial increase in DIC, resulting in longer periods of elevated pH and reduced pCO_2. Under such conditions, reduced growth of *Gephyrocapsa (Emiliania) huxleyi* was reported at pCO_2 values below ~100 µatm following NaOH addition (Faucher et al., 2025). Similar thresholds were observed for other key phytoplankton groups, particularly diatoms (Ferderer et al., 2024; Ferderer et al., 2025). Optimal growth occurred at pCO_2 values above ~120 µatm, with some observed negative effects at lower values. Together, these studies indicate that ecological responses to depend less on TA perturbation than on the magnitude and duration of high pH/low dissolved CO_2 perturbations.

Importantly though, these observations resulted from batch and mesocosm experiments with limited CO_2 ingassing. Limited CO_2 invasion likely prolonged exposure to low pCO_2 conditions for nearly 50 days in some cases (Ferderer et al., 2024; Goldenberg et al., 2024; Schneider et al., 2026). Such prolonged exposure may be representative of point-source alkalinity release, although dilution and CO_2 invasion will most likely decrease such duration. Our experiments support this assumption. In the absence of advection, reduced pCO_2 conditions persisted between one week and one month, although minimum pCO_2 values remained around 200 µatm following NaOH addition (Figs. 4 and 7). These concentrations remained close to reported optimal values for coccolithophore calcification in a large-scale mesocosm study (Schneider et al., 2026), suggesting, based on previously reported thresholds, that severe biological effects would have been unlikely under our experimental carbonate chemistry conditions. When advection was introduced, the CAP duration decreased substantially, which resulted in reduced pCO_2 conditions for only a few days. With pCO_2 returning to background values within three to six days, we hypothesise that, under higher gas-transfer velocities and corresponding equivalent wind speeds, atmospheric CO_2 invasion may decrease pH and replenish dissolved CO_2 concentrations more rapidly, substantially reducing environmental stress from OAE.

When considered together with previous (semi-)closed bottle and mesocosm experiments, our results indicate that studies conducted with limited CO_2 exchange may serve as an upper limit for quantifying biological responses to non-equilibrated OAE. In the open ocean, CO_2 ingassing and physical processes, particularly dilution and mixing, are expected to substantially decrease the CAP duration, thereby reducing the magnitude and duration of biological exposure to altered carbonate chemistry. Although this hypothesis is consistent with the observations reported here, it remains to be tested under realistic field conditions. Such testing will be important for assessing the environmental feasibility of large-scale OAE deployment. Several limitations should be considered when interpreting these findings. First, the experiments only reproduced simplified hydrodynamic conditions and did not fully capture the complexity of ocean turbulence, wave breaking, or horizontal and vertical transport. Second, repeated sampling progressively reduced the volume in each bottle, changing the headspace and potentially influencing gas exchange over time, although all treatments underwent the same sampling schedule. In addition, airflow rate and relative humidity were not measured at the individual outlets, and differences in headspace renewal among bottles therefore cannot be excluded. Nevertheless, disregarding biological processes, particle transport and large-scale dilution allowed physicochemical processes to be isolated. The results should therefore be interpreted as process-based laboratory observations that inform, rather than reproduce, field-scale OAE deployment.

Conclusion

This study presents the first six-month laboratory incubations for OAE using $Ca(OH)_2$, $Mg(OH)_2$ and NaOH, across a range of alkalinity additions and contrasting hydrodynamic conditions. Our results indicate that hydrodynamic conditions are a primary control on the realised efficiency of hydroxide-based OAE. Reduced advection limited mineral dissolution, favoured the persistence of supersaturated micro-environments around the dissolving particles, and reduced atmospheric CO_2 invasion through lower gas-transfer velocities. Ultimately, this resulted in lower realised alkalinity generation, a lower OAE efficiency and reduced CDR potential. In contrast, moderate advection enhanced mineral dissolution, accelerated CO_2 ingassing, shortened the CAP and limited efficiency losses due to secondary mineral formation. The CAP duration emerged as a useful indicator linking hydrodynamic conditions with the persistence of altered carbonate chemistry, the likelihood of secondary precipitation, and the duration of biological exposure to altered carbonate chemistry. Longer CAPs coincided with slower mineral dissolution, reduced gas exchange and prolonged supersaturation, thereby increasing the risk of $CaCO_3$ formation. Although the laboratory-derived gas-transfer velocities may not adequately represent natural conditions, our observations suggest that stronger mixing and more efficient gas exchange may reduce the CAP duration and improve realised alkalinity generation, although this hypothesis requires validation under realistic field conditions. These results also have implications for MRV protocols, because realised alkalinity generation cannot simply be inferred from feedstock dissolution alone. Processes such as mineral dissolution, CO_2 ingassing and secondary mineral formation all alter carbonate chemistry in different and sometimes opposite directions. Incorporating these coupled processes into future MRV frameworks is of primary importance for accurately quantifying realised CDR in field-scale deployments. Finally, the contrasting morphologies of $CaCO_3$ precipitates following $Ca(OH)_2$ and $Mg(OH)_2$ additions suggest feedstock-specific precipitation pathways and particle transport behaviour. These may further influence dissolution efficiency, secondary precipitation and alkalinity stability in the mixed layer, all relevant for CDR accounting. These processes remain poorly constrained in laboratory settings and should be studied under realistic hydrodynamic conditions, including water mixing, dilution, particle sinking and CO_2 equilibration. Better quantifying these coupled geochemical and physical processes will improve confidence in process-based models, reduce uncertainty in CDR estimates, and support the safe, effective and verifiable implementation of OAE at the field scale.

Appendix A

Figure A 1: Photograph of the setup with tubing maintained to each bottle rim with a binder clip. The air splitter apparatus can be distinguished in the background.

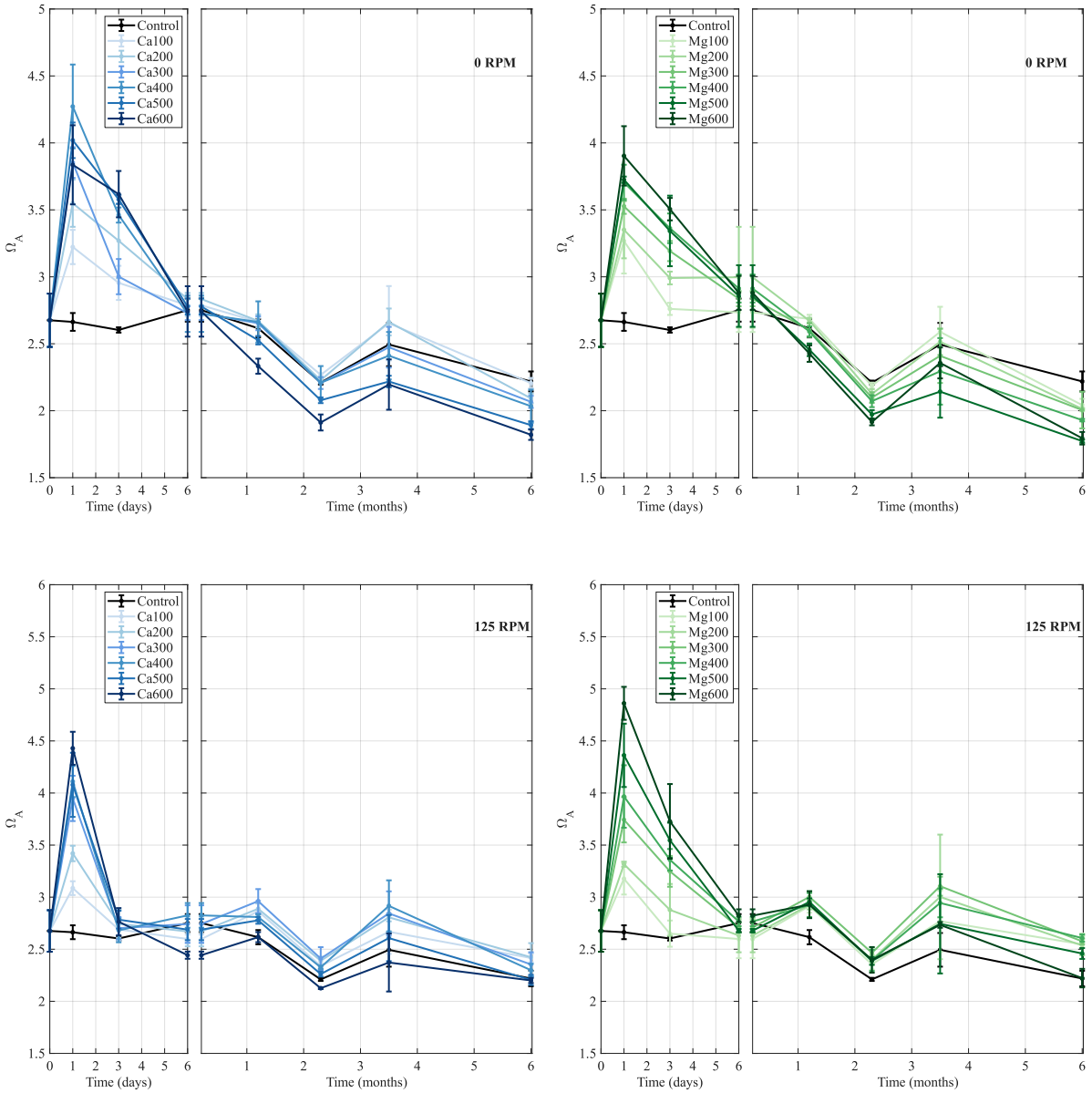

Figure A 2: Changes in Ω_A over time following $Ca(OH)_2$ (blue) or $Mg(OH)_2$ (green) additions with 0 RPM (top) and 125 RPM advection (bottom). The darker shades indicate higher alkaline material additions. Each point represents the mean of triplicates, with error bars representing one standard deviation of these three measurements.

Table A 1: Amount of material added per treatment and target TA (mean of triplicates ±standard deviation) in mg L^{-1}.

Treatment	+100	+200	+300	+400	+500	+600
0 RPM $Ca(OH)_2$	3.67 ±0.06	7.36 ±0.11	11.09 ±0.03	14.85 ±0.05	18.51 ±0.07	22.26 ±0.09
0 RPM $Mg(OH)_2$	2.88 ±0.05	5.85 ±0.09	8.72 ±0.06	11.71 ±0.07	14.57 ±0.04	17.46 ±0.07
125 RPM $Ca(OH)_2$	3.70 ±0.08	7.47 ±0.01	11.10 ±0.08	14.81 ±0.02	18.51 ±0.06	22.24 ±0.08
125 RPM $Mg(OH)_2$	2.95 ±0.04	5.84 ±0.10	8.73 ±0.06	11.61 ±0.05	14.63 ±0.12	17.54 ±0.10

Table A 2: Holm-adjusted one-sided p-values from planned post hoc treatment-control contrasts of the linear mixed-effects model, testing whether pCO_2 in each treatment was lower than that of the corresponding control at each sampling time. The Holm adjustment was applied across all treatment-control comparisons within each sampling time. Values in bold indicate statistically significant differences (adjusted p < 0.05). Adjusted p-values below 0.01 are reported as < 0.01.

0 RPM	**$Ca(OH)_2$**						**$Mg(OH)_2$**						**NaOH**
ΔTA	*100*	*200*	*300*	*400*	*500*	*600*	*100*	*200*	*300*	*400*	*500*	*600*	*600*
Day 1	**<0.01**	**<0.01**	**<0.01**	**<0.01**	**<0.01**	**<0.01**	**<0.01**	**<0.01**	**<0.01**	**<0.01**	**<0.01**	**<0.01**	**<0.01**
Day 3	**<0.01**	**<0.01**	**<0.01**	**<0.01**	**<0.01**	**<0.01**	**0.02**	**<0.01**	**<0.01**	**<0.01**	**<0.01**	**<0.01**	**<0.01**
Day 6	1.00	0.79	1.00	1.00	0.20	**0.03**	1.00	**0.03**	0.05	**0.01**	**<0.01**	**<0.01**	**<0.01**
Day 35	0.71	0.71	0.71	0.71	0.67	0.71	0.55	0.55	0.50	0.67	0.49	0.49	0.13
Day 69	1.00	1.00	1.00	1.00	1.00	1.00	1.00	1.00	1.00	1.00	1.00	1.00	1.00
Day 108	1.00	1.00	1.00	1.00	1.00	1.00	1.00	1.00	1.00	1.00	1.00	1.00	1.00
Day 174	1.00	1.00	1.00	1.00	1.00	1.00	1.00	1.00	1.00	1.00	1.00	1.00	1.00

125 RPM	**$Ca(OH)_2$**						**$Mg(OH)_2$**						**NaOH**
ΔTA	*100*	*200*	*300*	*400*	*500*	*600*	*100*	*200*	*300*	*400*	*500*	*600*	*600*
Day 1	**<0.01**	**<0.01**	**<0.01**	**<0.01**	**<0.01**	**<0.01**	**<0.01**	**<0.01**	**<0.01**	**<0.01**	**<0.01**	**<0.01**	**<0.01**
Day 3	1.00	1.00	1.00	1.00	1.00	1.00	1.00	1.00	**<0.01**	**<0.01**	**<0.01**	**<0.01**	**<0.01**
Day 6	1.00	1.00	1.00	1.00	1.00	1.00	1.00	1.00	1.00	1.00	1.00	1.00	1.00
Day 35	0.71	0.71	0.71	0.71	0.67	0.71	0.55	0.55	0.50	0.67	0.49	0.49	0.13

Day 69	1.00	1.00	1.00	1.00	1.00	1.00	1.00	1.00	1.00	1.00	1.00	1.00	1.00
Day 108	0.19	0.16	0.10	**0.01**	0.17	0.24	0.15	**0.02**	**<0.01**	**0.01**	0.31	0.20	0.88
Day 174	1.00	1.00	1.00	1.00	1.00	0.33	1.00	1.00	1.00	1.00	1.00	1.00	1.00

Data availability

The data will be made available in a public repository upon acceptance of the manuscript for publication.

Author contributions

CAM designed the experiments with input from JH. CAM and MSM ran the experiments. CAM and PB performed the analyses. CAM wrote the first draft of the manuscript, and inputs from JH, MSM, and PB led to the final version of the manuscript.

Competing interests

JH serves as a consultant for the Planeteers GmbH. All authors declare that they have no competing interests.

Acknowledgements

The authors would like to thank Prof. Douglas Wallace from Dalhousie University, Canada, for his early advice on the experimental setup, Assoc. Prof. Ruth Musgrave for her inputs on gas-transfer-velocity calculations, and the broader Ocean Alk-align team for their input during online meetings. The authors would also like to thank Dr Niko Lahajnar for accommodating laboratory space, Dr Dirk Eifler and Nuray Eroglu for their support with F-AAS analyses, and Tom Jäppinen for his support with Bettersizer analyses. The authors acknowledge the use of AI-assisted tools for literature searches and for grammatical and spelling revision of the manuscript. All relevant outputs were subsequently checked, reviewed and verified before consideration for in-text incorporation by the authors.

Financial support

This research has been supported by the Ocean Alk-Align project funded by the Carbon to Sea Initiative, and by the German Federal Ministry of Education and Research through the CDRmare project RETAKE-II (grant no. 03F0965F).

References

Bach, L. T., Tyka, M. D., Wang, B., and Fennel, K.: Lethal by design? Guiding environmental assessments of ocean alkalinity enhancement toward realistic contextualization of the alkalinity perturbation, CDRXIV, 10.70212/cdrxiv.2025457.v1, 2025.

Bach, L. T.: The additionality problem of ocean alkalinity enhancement, Biogeosciences, 21, 261-277, 10.5194/bg-21-261-2024, 2024.

Bach, L. T., Gill, S. J., Rickaby, R. E. M., Gore, S., and Renforth, P.: CO_2 removal with enhanced weathering and Ocean Alkalinity Enhancement: Potential risks and co-benefits for marine pelagic ecosystems, Frontiers in Climate, 1, 10.3389/fclim.2019.00007, 2019.

Badocco, D., Pedrini, F., Pastore, A., di Marco, V., Marin, M. G., Bogialli, S., Roverso, M., and Pastore, P.: Use of a simple empirical model for the accurate conversion of the seawater pH value measured with NIST calibration into seawater pH scales, Talanta, 225, 122051, 10.1016/j.talanta.2020.122051, 2021.

Baltruschat, S., Hartmann, J., Suitner, N., Moras, C. A., Lim, C., Bastianini, L., and Renforth, P.: Assessment of solid ikaite release into seawater – implications for ocean alkalinity enhancement, Applied Geochemistry, 203, 106781, 10.1016/j.apgeochem.2026.106781, 2026.

Beck, R. and Andreassen, J.-P.: Spherulitic Growth of Calcium Carbonate, Crystal Growth & Design, 10, 2934-2947, 10.1021/cg901460g, 2010.

Caserini, S., Pagano, D., Campo, F., Abbà, A., De Marco, S., Righi, D., Renforth, P., and Grosso, M.: Potential of maritime transport for ocean liming and atmospheric CO_2 removal, Frontiers in Climate, 3, 10.3389/fclim.2021.575900, 2021.

Chave, K. E. and Suess, E.: Calcium carbonate saturation in seawater: Effects of dissolved organic matter, Limnology and Oceanography, 15, 633-637, 10.4319/lo.1970.15.4.0633, 1970.

Cushman-Roisin, B. and Beckers, J.-M.: Chapter 20 - Oceanic General Circulation, in: International Geophysics, edited by: Cushman-Roisin, B., and Beckers, J.-M., Academic Press, 657-699, 10.1016/B978-0-12-088759-0.00020-1, 2011.

Dale, A. W., Geilert, S., Diercks, I., Fuhr, M., Perner, M., Scholz, F., and Wallmann, K.: Seafloor alkalinity enhancement as a carbon dioxide removal strategy in the Baltic Sea, Communications Earth & Environment, 5, 452, 10.1038/s43247-024-01569-3, 2024.

Dickson, A. G.: Standard potential of the reaction: $AgCl(s) + 12H_2(g) = Ag(s) + HCl(aq)$, and the standard acidity constant of the ion HSO_4^- in synthetic sea water from 273.15 to 318.15 K, The Journal of Chemical Thermodynamics, 22, 113-127, 10.1016/0021-9614(90)90074-Z, 1990.

Dickson, A. G.: Standards for ocean measurements, Oceanography, 23, 34-47, 10.5670/oceanog.2010.22, 2010.

Dickson, A. G., Sabine, C. L., and Christian, J. R.: Guide to best practices for ocean CO_2 measurements, PICES Special Publication 3; IOCCP Report 8, Sidney, British Columbia, North Pacific Marine Science Organization, 191 pp., 10.25607/OBP-1342, 2007.

Drever, J. I.: The Geochemistry of Natural Waters, 3rd, Surface and Groundwater Environments, Prentice Hall, 1997.

Eisaman, M. D., Geilert, S., Renforth, P., Bastianini, L., Campbell, J., Dale, A. W., Foteinis, S., Grasse, P., Hawrot, O., Löscher, C. R., Rau, G. H., and Rønning, J.: Assessing the technical aspects of ocean-alkalinity-enhancement approaches, Guide to Best Practices in Ocean Alkalinity Enhancement Research, 2-oae2023, 3, 10.5194/sp-2-oae2023-3-2023, 2023.

England, P. I. and Bach, L. T.: Influence of Wave Action on Applications of Olivine-Based Ocean Alkalinity Enhancement on Sandy Beaches, Geophysical Research Letters, 52, e2025GL114922, 10.1029/2025GL114922, 2025.

European Parliament and Council of the European Union: Directive 2000/60/EC of the European Parliament and of the Council of 23 October 2000 establishing a framework for Community action in the field of water policy, Official Journal of the European Communities OJ L 327, 1–73, 22/12/2000 (consolidated version: 10/05/2026), 2000.

Faucher, G., Haunost, M., Paul, A. J., Tietz, A. U. C., and Riebesell, U.: Growth response of Emiliania huxleyi to ocean alkalinity enhancement, Biogeosciences, 22, 405-415, 10.5194/bg-22-405-2025, 2025.

Ferderer, A., Chase, Z., Kennedy, F., Schulz, K. G., and Bach, L. T.: Assessing the influence of ocean alkalinity enhancement on a coastal phytoplankton community, Biogeosciences, 19, 5375-5399, 10.5194/bg-19-5375-2022, 2022.

Ferderer, A., Schulz, K. G., Riebesell, U., Baker, K. G., Chase, Z., and Bach, L. T.: Investigating the effect of silicate- and calcium-based ocean alkalinity enhancement on diatom silicification, Biogeosciences, 21, 2777-2794, 10.5194/bg-21-2777-2024, 2024.

Ferderer, A., Schulz, K. G., Willis, A., Baker, K. G., Chase, Z., and Bach, L. T.: Carbonate chemistry fitness landscapes inform diatom resilience to future perturbations, Science Advances, 11, eadu8024, 10.1126/sciadv.adu8024, 2025.
Flipkens, G., Fuhr, M., Fiers, G., Meysman, F. J. R., Town, R. M., and Blust, R.: Enhanced olivine dissolution in seawater through continuous grain collisions, Geochimica et Cosmochimica Acta, 359, 84-99, 10.1016/j.gca.2023.09.002, 2023.
Foteinis, S., Andresen, J., Campo, F., Caserini, S., and Renforth, P.: Life cycle assessment of ocean liming for carbon dioxide removal from the atmosphere, Journal of Cleaner Production, 370, 133309, 10.1016/j.jclepro.2022.133309, 2022.
Frew, N. M., Glover, D. M., Bock, E. J., and McCue, S. J.: A new approach to estimation of global air-sea gas transfer velocity fields using dual-frequency altimeter backscatter, Journal of Geophysical Research: Oceans, 112, 10.1029/2006JC003819, 2007.
Fuhr, M., Geilert, S., Schmidt, M., Liebetrau, V., Vogt, C., Ledwig, B., and Wallmann, K.: Kinetics of Olivine Weathering in Seawater: An Experimental Study, Frontiers in Climate, 4, 10.3389/fclim.2022.831587, 2022.
Fuhr, M., Wallmann, K., Dale, A. W., Diercks, I., Kalapurakkal, H. T., Schmidt, M., Sommer, S., Böhnke, S., Perner, M., and Geilert, S.: Disentangling artificial and natural benthic weathering in organic rich Baltic Sea sediments, Frontiers in Climate, 5, 2023, 10.3389/fclim.2023.1245580, 2023.
Fuhr, M., Wallmann, K., Dale, A. W., Kalapurakkal, H. T., Schmidt, M., Sommer, S., Deusner, C., Spiegel, T., Kowalski, J., and Geilert, S.: Alkaline mineral addition to anoxic to hypoxic Baltic Sea sediments as a potentially efficient CO2-removal technique, Frontiers in Climate, 6, 2024, 10.3389/fclim.2024.1338556, 2024.
Fuhr, M., Dale, A. W., Wallmann, K., Bährle, R., Kalapurakkal, H. T., Sommer, S., Spiegel, T., Dobashi, R., Buchholz, B., Schmidt, M., Perner, M., and Geilert, S.: Calcite is an efficient and low-cost material to enhance benthic weathering in shelf sediments of the Baltic Sea, Communications Earth & Environment, 6, 106, 10.1038/s43247-025-02079-6, 2025.
Fuss, S., Lunstrum, A., Prütz, R., and Gruner, F.: Chapter 10: Costs and Potentials, in: The State of Carbon Dioxide Removal 3rd Edition 2026 (eds. Edwards, M. R. et al.), 10.17605/OSF.IO/FBZ4X, 2026.
Goldenberg, S. U., Riebesell, U., Brüggemann, D., Börner, G., Sswat, M., Folkvord, A., Couret, M., Spjelkavik, S., Sánchez, N., Jaspers, C., and Moyano, M.: Early life stages of fish under ocean alkalinity enhancement in coastal plankton communities, Biogeosciences, 21, 4521-4532, 10.5194/bg-21-4521-2024, 2024.
Gránásy, L., Pusztai, T., Tegze, G., Warren, J. A., and Douglas, J. F.: Growth and form of spherulites, Physical Review E, 72, 011605, 10.1103/PhysRevE.72.011605, 2005.
Griskey, R. G.: Fluid Flow Basic Equations, in: Transport Phenomena and Unit Operations: A Combined Approach, John Wiley & Sons, 23-54, 10.1002/0471722057, 2002.
Haas, A. R.: The effect of the addition of alkali to sea water upon the hydrogen ion concentration, Journal of Biological Chemistry, 26, 515-517, 10.1016/S0021-9258(18)87433-6, 1916.
Hartmann, J., Suitner, N., Lim, C., Schneider, J., Marín-Samper, L., Arístegui, J., Renforth, P., Taucher, J., and Riebesell, U.: Stability of alkalinity in ocean alkalinity enhancement (OAE) approaches – consequences for durability of CO_2 storage, Biogeosciences, 20, 781-802, 10.5194/bg-20-781-2023, 2023.
Hashim, M. S., Marx, L., Klein, F., Dean, C. L., Burdige, E., Hayden, M., McCorkle, D. C., and Subhas, A. V.: Mineral formation during shipboard ocean alkalinity enhancement experiments in the North Atlantic, Biogeosciences, 22, 7149-7165, 10.5194/bg-22-7149-2025, 2025.
Hausfather, Z.: An assessment of current policy scenarios over the 21st century and the reduced plausibility of high-emissions pathways, Dialogues on Climate Change, 2, 26-32, 10.1177/29768659241304854, 2025.
Ho, D. T., Law, C. S., Smith, M. J., Schlosser, P., Harvey, M., and Hill, P.: Measurements of air-sea gas exchange at high wind speeds in the Southern Ocean: Implications for global parameterizations, Geophysical Research Letters, 33, 10.1029/2006GL026817, 2006.
IPCC: Summary for Policymakers. In: Climate Change 2021: The Physical Science Basis. Contribution of Working Group I to the Sixth Assessment Report of the Intergovernmental Panel on Climate Change [Masson-Delmotte, V., P. Zhai, A. Pirani, S.L. Connors, C. Péan, S. Berger, N. Caud, Y. Chen, L. Goldfarb, M.I. Gomis, M. Huang, K. Leitzell, E. Lonnoy, J.B.R. Matthews, T.K. Maycock, T. Waterfield, O. Yelekçi, R. Yu, and B. Zhou (eds.)], Cambridge University Press, Cambridge, United Kingdom and New York, NY, USA, pp. 3-32, 10.1017/9781009157896.001, 2021.
IPCC: Summary for Policymakers. In: Climate Change 2022: Impacts, Adaptation and Vulnerability. Contribution of Working Group II to the Sixth Assessment Report of the Intergovernmental Panel on Climate Change [H.-O. Pörtner, D.C. Roberts, M. Tignor, E.S. Poloczanska, K. Mintenbeck, A. Alegría, M. Craig, S. Langsdorf, S. Löschke, V. Möller, A. Okem, B. Rama

(eds.)], Cambridge University Press, Cambridge, United Kingdom and New York, NY, USA, pp. 3–33, 10.1017/9781009325844.001, 2022.
Isometric: Ocean Alkalinity Enhancement from Coastal Outfalls, Isometric, Version 1.1, 2026.
Jones, D. C., Ito, T., Takano, Y., and Hsu, W.-C.: Spatial and seasonal variability of the air-sea equilibration timescale of carbon dioxide, Global Biogeochemical Cycles, 28, 1163-1178, 10.1002/2014GB004813, 2014.
Kapp, E. M.: The Precipitation of Calcium and Magnesium from Sea Water by Sodium Hydroxide, Biological Bulletin, 55, 453-458, 10.2307/1536800, 1928.
Kauk, S.: World's first verified Ocean Alkalinity Enhancement credits: https://isometric.com/writing-articles/worlds-first-verified-ocean-alkalinity-enhancement-credits (last access: 14 July 2026), 2025.
Kheshgi, H. S.: Sequestering atmospheric carbon dioxide by increasing ocean alkalinity, Energy, 20, 915-922, 10.1016/0360-5442(95)00035-F, 1995.
Kousoulas, K., Ferderer, A., Eriksen, R., and Bach, L. T.: Winners and losers under hydroxide-based ocean alkalinity enhancement in a Tasmanian plankton community, Journal of Phycology, 61, 989-1006, 10.1111/jpy.70052, 2025.
Lasaga, A. C.: Kinetic Theory in the Earth Sciences, Princeton University Press, Princeton, 10.1515/9781400864874, 2014.
Lee, K., Kim, T.-W., Byrne, R. H., Millero, F. J., Feely, R. A., and Liu, Y.-M.: The universal ratio of boron to chlorinity for the North Pacific and North Atlantic oceans, Geochimica et Cosmochimica Acta, 74, 1801-1811, 10.1016/j.gca.2009.12.027, 2010.
Lee, C.-H., Subhas, A. V., Kim, J.-H., and Lee, K.: Ocean Carbon Dioxide Removal and Storage, Chemical Reviews, 126, 1110-1144, 10.1021/acs.chemrev.5c00433, 2026.
Levich, V. G.: Physicochemical hydrodynamics, Prentice-Hall, 1962.
Lewis, E. L. and Perkin, R. G.: The practical salinity scale 1978: conversion of existing data, Deep Sea Research Part A. Oceanographic Research Papers, 28, 307-328, 10.1016/0198-0149(81)90002-9, 1981.
Lunstrum, A., Keller, D., Hartmann, J., and Moras, C. A.: A framework for understanding efficiency losses of Ocean Alkalinity Enhancement, CDRXIV [preprint], 10.70212/cdrxiv.2026517.v1, 2026.
Marion, G. M., Millero, F. J., and Feistel, R.: Precipitation of solid phase calcium carbonates and their effect on application of seawater S_A - T - P models, Ocean Science, 5, 285-291, 10.5194/os-5-285-2009, 2009.
Meysman, F. J. R. and Montserrat, F.: Negative CO2 emissions via enhanced silicate weathering in coastal environments, Biology Letters, 13, 20160905, 10.1098/rsbl.2016.0905, 2017.
Miller, S. D., Marandino, C., and Saltzman, E. S.: Ship-based measurement of air-sea CO2 exchange by eddy covariance, Journal of Geophysical Research: Atmospheres, 115, 10.1029/2009JD012193, 2010.
Millero, F. J. and Poisson, A.: International one-atmosphere equation of state of seawater, Deep Sea Research Part A. Oceanographic Research Papers, 28, 625-629, 10.1016/0198-0149(81)90122-9, 1981.
Montserrat, F., Renforth, P., Hartmann, J., Leermakers, M., Knops, P., and Meysman, F. J. R.: Olivine dissolution in seawater: Implications for CO2 sequestration through enhanced weathering in coastal environments, Environmental Science & Technology, 51, 3960-3972, 10.1021/acs.est.6b05942, 2017.
Moras, C. A., Bach, L. T., Cyronak, T., Joannes-Boyau, R., and Schulz, K. G.: Ocean alkalinity enhancement – avoiding runaway $CaCO_3$ precipitation during quick and hydrated lime dissolution, Biogeosciences, 19, 3537-3557, 10.5194/bg-19-3537-2022, 2022.
Moras, C. A., Bach, L. T., Cyronak, T., Joannes-Boyau, R., and Schulz, K. G.: Preparation and quality control of in-house reference materials for marine dissolved inorganic carbon and total alkalinity measurements, Limnology and Oceanography: Methods, 10.1002/lom3.10570, 2023.
Moras, C. A., Cyronak, T., Bach, L. T., Joannes-Boyau, R., and Schulz, K. G.: Effects of grain size and seawater salinity on magnesium hydroxide dissolution and secondary calcium carbonate precipitation kinetics: implications for ocean alkalinity enhancement, Biogeosciences, 21, 3463-3475, 10.5194/bg-21-3463-2024, 2024.
Morse, J. W., Arvidson, R. S., and Lüttge, A.: Calcium carbonate formation and dissolution, Chemical Reviews, 107, 342-381, 10.1021/cr050358j, 2007.
Morse, J. W., Wang, Q., and Tsio, M. Y.: Influences of temperature and Mg:Ca ratio on $CaCO_3$ precipitates from seawater, Geology, 25, 85-87, 10.1130/0091-7613(1997)025<0085:Iotamc>2.3.Co;2, 1997.
Pan, Y., Li, Y., Ma, Q., He, H., Wang, S., Sun, Z., Cai, W.-J., Dong, B., Di, Y., Fu, W., and Chen, C.-T. A.: The role of Mg^{2+} in inhibiting $CaCO_3$ precipitation from seawater, Marine Chemistry, 237, 104036, 10.1016/j.marchem.2021.104036, 2021.

Oschlies, A., Bach, L. T., Rickaby, R. E. M., Satterfield, T., Webb, R., and Gattuso, J. P.: Climate targets, carbon dioxide removal, and the potential role of ocean alkalinity enhancement, Guide to Best Practices in Ocean Alkalinity Enhancement Research, 2-oae2023, 1, 10.5194/sp-2-oae2023-1-2023, 2023.

Paul, A. J., Haunost, M., Goldenberg, S. U., Hartmann, J., Sánchez, N., Schneider, J., Suitner, N., and Riebesell, U.: Ocean alkalinity enhancement in an open-ocean ecosystem: biogeochemical responses and carbon storage durability, Biogeosciences, 22, 2749-2766, 10.5194/bg-22-2749-2025, 2025.

Perez, F. F. and Fraga, F.: Association constant of fluoride and hydrogen ions in seawater, Marine Chemistry, 21, 161-168, 10.1016/0304-4203(87)90036-3, 1987.

Pytkowicz, R. M.: Rates of inorganic calcium carbonate nucleation, The Journal of Geology, 73, 196-199, 10.1086/627056, 1965.

Ramírez, L., Pozzo-Pirotta, L. J., Trebec, A., Manzanares-Vázquez, V., Díez, J. L., Arístegui, J., Riebesell, U., Archer, S. D., and Segovia, M.: Ocean alkalinity enhancement (OAE) does not cause cellular stress in a phytoplankton community of the subtropical Atlantic Ocean, Biogeosciences, 22, 1865-1886, 10.5194/bg-22-1865-2025, 2025.

Reynolds, O.: XXIX. An experimental investigation of the circumstances which determine whether the motion of water shall be direct or sinuous, and of the law of resistance in parallel channels, Philosophical Transactions of the Royal Society of London, 935-982, 10.1098/rstl.1883.0029, 1883.

Rigopoulos, I., Harrison, A. L., Delimitis, A., Ioannou, I., Efstathiou, A. M., Kyratsi, T., and Oelkers, E. H.: Carbon sequestration via enhanced weathering of peridotites and basalts in seawater, Applied Geochemistry, 91, 197-207, 10.1016/j.apgeochem.2017.11.001, 2018.

Risien, C. M. and Chelton, D. B.: A Global Climatology of Surface Wind and Wind Stress Fields from Eight Years of QuikSCAT Scatterometer Data, Journal of Physical Oceanography, 38, 2379-2413, 10.1175/2008JPO3881.1, 2008.

Rushdi, A. I., Pytkowicz, R. M., Suess, E., and Chen, C. T.: The effects of magnesium-to-calcium ratios in artificial seawater, at different ionic products, upon the induction time, and the mineralogy of calcium carbonate: A laboratory study, Geologische Rundschau, 81, 571-578, 10.1007/BF01828616, 1992.

Saez Moreno, M., Hartmann, J., Börker, J., Bartsch, P., and Moras, C. A.: The role of temperature and salinity on ocean alkalinity enhancement performance, EGUsphere, 2026, 1-30, 10.5194/egusphere-2026-3277, 2026.

Schneider, J., Riebesell, U., Moras, C. A., Marín-Samper, L., Kittu, L. R., Ortíz-Cortes, J., and Schulz, K. G.: Carbon fixation of a temperate plankton community in response to calcium- and silicate-based Ocean Alkalinity Enhancement using air-sea gas exchange measurements, Biogeosciences, 23, 137-153, 10.5194/bg-23-137-2026, 2026.

Schockman, K. M. and Byrne, R. H.: Spectrophotometric determination of the bicarbonate dissociation constant in seawater, Geochimica et Cosmochimica Acta, 300, 231-245, 10.1016/j.gca.2021.02.008, 2021.

Schulz, K. G., Bach, L. T., and Dickson, A. G.: Seawater carbonate system considerations for ocean alkalinity enhancement research, State Planet Discuss., 2023, 1-24, 10.5194/sp-2023-12, 2023.

Sharqawy, M. H., Lienhard, J. H., and Zubair, S. M.: Thermophysical properties of seawater: a review of existing correlations and data, Desalination and Water Treatment, 16, 354-380, 10.5004/dwt.2010.1079, 2010.

Shaw, C., Ringham, M. C., Carter, B. R., Tyka, M. D., and Eisaman, M. D.: Using magnesium hydroxide for ocean alkalinity enhancement: elucidating the role of formation conditions on material properties and dissolution kinetics, Frontiers in Climate, 7, 2025, 10.3389/fclim.2025.1616362, 2025.

Suitner, N., Hartmann, J., Varliero, S., Faucher, G., Suessle, P., and Moras, C. A.: Surface area and Ω-aragonite oversaturation as controls of the runaway precipitation process in ocean alkalinity enhancement, Biogeosciences, 23, 3965-3980, 10.5194/bg-23-3965-2026, 2026.

Suitner, N., Faucher, G., Lim, C., Schneider, J., Moras, C. A., Riebesell, U., and Hartmann, J.: Ocean alkalinity enhancement approaches and the predictability of runaway precipitation processes: results of an experimental study to determine critical alkalinity ranges for safe and sustainable application scenarios, Biogeosciences, 21, 4587-4604, 10.5194/bg-21-4587-2024, 2024.

Sulpis, O., Mucci, A., Boudreau, B. P., Barry, M. A., and Johnson, B. D.: Controlling the diffusive boundary layer thickness above the sediment–water interface in a thermostated rotating-disk reactor, Limnology and Oceanography: Methods, 17, 241-253, 10.1002/lom3.10309, 2019.

Tang, H., Wu, X., Xian, H., Zhu, J., Wei, J., Liu, H., and He, H.: Heterogeneous nucleation and growth of $CaCO_3$ on calcite (104) and aragonite (110) surfaces: Implications for the formation of abiogenic carbonate cements in the ocean, Minerals, 10, 294, 10.3390/min10040294, 2020.

Thorpe, S. A.: An Introduction to Ocean Turbulence, Cambridge University Press, Cambridge, 10.1017/CBO9780511801198, 2007.

Tokinaga, H. and Xie, S.-P.: Wave- and Anemometer-Based Sea Surface Wind (WASWind) for Climate Change Analysis, Journal of Climate, 24, 267-285, 10.1175/2010JCLI3789.1, 2011.

Tracy, S. L., Williams, D. A., and Jennings, H. M.: The growth of calcite spherulites from solution: II. Kinetics of formation, Journal of Crystal Growth, 193, 382-388, 10.1016/S0022-0248(98)00521-1, 1998.

U.S. Environmental Protection Agency: National Recommended Water Quality Criteria - Aquatic Life Criteria Table: https://www.epa.gov/wqc/national-recommended-water-quality-criteria-aquatic-life-criteria-table (last access: 14 July 2026), 2026.

U.S. Environmental Protection Agency: Quality Criteria for Water 1986, U.S. Environmental Protection Agency, Washington, DC, EPA 440/5-86-001, 1986.

Varliero, S., Buono, A., Caserini, S., Raos, G., and Macchi, P.: Chemical Aspect of Ocean Liming for CO2 Removal: Dissolution Kinetics of Calcium Hydroxide in Seawater, ACS Engineering Au, 4, 422-431, 10.1021/acsengineeringau.4c00008, 2024.

Wanninkhof, R.: Relationship between wind speed and gas exchange over the ocean revisited, Limnology and Oceanography: Methods, 12, 351-362, 10.4319/lom.2014.12.351, 2014.

Weiss, R. F.: Carbon dioxide in water and seawater: the solubility of a non-ideal gas, Marine Chemistry, 2, 203-215, 10.1016/0304-4203(74)90015-2, 1974.

Yang, B., Leonard, J., and Langdon, C.: Seawater alkalinity enhancement with magnesium hydroxide and its implication for carbon dioxide removal, Marine Chemistry, 253, 104251, 10.1016/j.marchem.2023.104251, 2023.

Yu, T., He, Y., and Yan, X.: Global air-sea surface carbon dioxide transfer velocity and flux estimated using 17 a altimeter data and a new algorithm, Acta Oceanologica Sinica, 32, 24-33, 10.1007/s13131-013-0362-9, 2013.

Zeebe, R. E. and Wolf-Gladrow, D.: CO_2 in seawater: equilibrium, kinetics, isotopes, 65, Gulf Professional Publishing, 360 pp., 2001.

Zhou, X., Reichl, B. G., Romero, L., and Deike, L.: A Sea State Dependent Gas Transfer Velocity for CO2 Unifying Theory, Model, and Field Data, Earth and Space Science, 10, e2023EA003237, 10.1029/2023EA003237, 2023.

Zhou, M., Tyka, M. D., Ho, D. T., Yankovsky, E., Bachman, S., Nicholas, T., Karspeck, A. R., and Long, M. C.: Mapping the global variation in the efficiency of ocean alkalinity enhancement for carbon dioxide removal, Nature Climate Change, 15, 59-65, 10.1038/s41558-024-02179-9, 2025.

Zubovic, K. P., Horvath, A., Brien, D. M., Rateau, R., Terribili, L., Winters, S., Docaigne, E., Guyett, P. C., and Rodriguez-Blanco, J. D.: Crystallisation of CaCO3 polymorphs induced by layered PET-based microplastic particles, Environmental Sciences Europe, 37, 52, 10.1186/s12302-025-01090-0, 2025.